

# Beyond the T Dwarfs: Theoretical Spectra, Colors, and Detectability of the Coolest Brown Dwarfs

Adam Burrows<sup>1</sup>, David Sudarsky<sup>1</sup>, & Jonathan I. Lunine<sup>2</sup>

## ABSTRACT

We explore the spectral and atmospheric properties of brown dwarfs cooler than the latest known T dwarfs. Our focus is on the yet-to-be-discovered free-floating brown dwarfs in the  $T_{\text{eff}}$  range from  $\sim 800$  K to  $\sim 130$  K and with masses from 25 to 1  $M_{\text{J}}$ . This study is in anticipation of the new characterization capabilities enabled by the launch of SIRTF and the eventual launch of JWST. In addition, it is in support of the continuing ground-based searches for the coolest substellar objects. We provide spectra from  $\sim 0.4$   $\mu\text{m}$  to 30  $\mu\text{m}$ , highlight the evolution and mass dependence of the dominant  $\text{H}_2\text{O}$ ,  $\text{CH}_4$ , and  $\text{NH}_3$  molecular bands, consider the formation and effects of water-ice clouds, and compare our theoretical flux densities with the putative sensitivities of the instruments on board SIRTF and JWST. The latter can be used to determine the detection ranges from space of cool brown dwarfs. In the process, we determine the reversal point of the blueward trend in the near-infrared colors with decreasing  $T_{\text{eff}}$  (a prominent feature of the hotter T dwarf family), the  $T_{\text{eff}}$ s at which water and ammonia clouds appear, the strengths of gas-phase ammonia and methane bands, the masses and ages of the objects for which the neutral alkali metal lines (signatures of L and T dwarfs) are muted, and the increasing role as  $T_{\text{eff}}$  decreases of the mid-infrared fluxes longward of 4  $\mu\text{m}$ . These changes suggest physical reasons to expect the emergence of at least one new stellar class beyond the T dwarfs. Furthermore, studies in the mid-infrared could assume a new, perhaps transformational, importance in the understanding of the coolest brown dwarfs. Our spectral models populate, with cooler brown dwarfs having progressively more planet-like features, the theoretical gap between the known T dwarfs and the known giant planets. Such objects likely inhabit the galaxy, but their numbers are as yet unknown.

*Subject headings:* general—stars: low-mass, brown dwarfs—radiative transfer—molecular processes—infrared: stars

---

<sup>1</sup>Department of Astronomy and Steward Observatory, The University of Arizona, Tucson, AZ 85721

<sup>2</sup>Lunar and Planetary Laboratory, The University of Arizona, Tucson, AZ 85721

## 1. Introduction

The discovery of Gliese 229B (Oppenheimer et al. 1995) and the successes of the 2MASS (Reid 1994; Stiening, Skrutskie, and Capps 1995), Sloan (Strauss et al. 1999), and DENIS (Delfosse et al. 1997) surveys have collectively opened up a new chapter in stellar astronomy. The L and T dwarfs (Kirkpatrick et al. 1999,2000; Martín et al. 1999; Burgasser et al. 1999, 2000a,b,c) that have thereby been discovered and characterized comprise the first new “stellar” types to be added to the stellar zoo in nearly 100 years. The lower edge of the solar-metallicity main sequence is an L dwarf not an M dwarf, with a  $T_{\text{eff}}$  near 1700 Kelvin (K), and more than 200 L dwarfs spanning a  $T_{\text{eff}}$  range from  $\sim 2200$  K to  $\sim 1300$  K are now inventoried. The coolest L dwarfs are also brown dwarfs, objects too light ( $\lesssim 0.074 M_{\odot}$ ) to ignite hydrogen stably on the main sequence (Burrows et al. 2001). Similarly, to date approximately 40 T dwarfs have been discovered spanning the  $T_{\text{eff}}$  range from  $\sim 1200$  K to  $\sim 750$  K. These are all brown dwarfs and are the coldest “stars” currently known.

However, the edge of the “stellar” mass function in the field, in the solar neighborhood, or in star clusters has not yet been reached and it is strongly suspected that in the wide mass and  $T_{\text{eff}}$  gap between the currently known T dwarfs and Jovian-like planets there resides a population of very cool ( $150 \text{ K} < T_{\text{eff}} < 800 \text{ K}$ ) brown dwarfs. Such objects could be too dim in the optical and near-infrared to have been seen with current technology, but might be discovered in the not-too-distant future by the NGSS/WISE infrared space survey (Wright et al. 2001), SIRTF (Space InfraRed Telescope Facility; Werner and Fanson 1995), and/or JWST (James Webb Space Telescope; Mather and Stockman 2000). In this paper, we calculate the spectra and colors of such a population in order to provide a theoretical underpinning for the future study of these coolest of brown dwarfs. Dwelling as they do at  $T_{\text{eff}}$ s beyond those of the currently-known T dwarfs, these “stars” emit strongly in the near- and mid-infrared. Consequently, we highlight their fluxes from 1 to 30 microns and compare these fluxes with the putative sensitivities of instruments on SIRTF and planned instruments on JWST. We include the effects of water clouds that form in the coolest of these objects. The presence of clouds of any sort emphasizes the kinship of this transitional class with solar system planets, in which clouds play a prominent role. (Note, however, that on Jupiter itself water clouds are too deep below the ammonia cloud layer to have been unambiguously detected.)

Since we focus on isolated free-floaters or wide binary brown dwarfs, we do not include external irradiation by companions. The  $T_{\text{eff}}$ s of this model set ( $\leq 800$  K) are such that silicate and iron clouds are deeply buried. Hence, unlike for L dwarfs and early T dwarfs (Marley et al. 2002; Burrows et al. 2002), the effect of such refractory clouds on emergent spectra can be ignored. In §2, we discuss our numerical approaches and inputs. We go on in §3 to describe our mass-age model set and our use of the Burrows et al. (1997) evolutionary calculations to provide the mapping between ( $T_{\text{eff}}$ , gravity [ $g$ ]) and (mass, age). In §4, we present a representative sample of derived atmospheric temperature( $T$ )/pressure( $P$ ) profiles and their systematics. This leads in §5 to a short discussion of the SIRTF and JWST point-source sensitivities. Section 6 concerns the derived spectra and is the central section of the paper. In it, we discuss prominent spectral

features from the optical to 30 microns, trends as a function of age,  $T_{\text{eff}}$ , and mass, diagnostics of particular atmospheric constituents, and detectability with instruments on SIRTf and JWST. We find that these platforms can in principle detect brown dwarfs cooler than the current T dwarfs out to large distances. We also explore the evolution of  $J - K$  and its eventual return to the “red” (Marley et al. 2002; Stephens, Marley, and Noll 2001), reversing the blueward trend with decreasing  $T_{\text{eff}}$  that roughly characterizes the known T dwarfs. Furthermore, we make suggestions for filter sets that may optimize their study with NIRCcam on JWST. Finally, we present physical reasons for anticipating the emergence of a new stellar type beyond the T dwarfs. In §7, we summarize what we have determined about this coolest-dwarf family and the potential for their detection.

## 2. Numerical Tools and Assumptions

To calculate model atmospheres of cool brown dwarfs requires 1) a method to solve the radiative transfer, radiative equilibrium, and hydrostatic equilibrium equations, 2) a convective algorithm, 3) an equation of state that also provides the molecular and atomic compositions, 4) a method to model clouds that may form, and 5) an extensive opacity database for the constituents that arise in low-temperature, high-pressure atmospheres. The computer program we use to solve the atmosphere and spectrum problem in a fully self-consistent fashion is an updated version of the planar code TLUSTY (Hubeny 1988; Hubeny & Lanz 1995), which uses a hybrid of Complete Linearization and Accelerated Lambda Iteration (Hubeny 1992). To handle convection, we use mixing-length theory (with a mixing length equal to one pressure-scale height). The equation of state we use to find the P/T/density( $\rho$ ) relation is that of Saumon, Chabrier, and Van Horn (1995) and the molecular compositions are calculated using a significantly updated version of the code SOLGASMIX (Burrows and Sharp 1999). The latter incorporates a rainout algorithm for refractory silicates and iron (Burrows et al. 2001). The most important molecules are  $\text{H}_2$ ,  $\text{H}_2\text{O}$ ,  $\text{CH}_4$ ,  $\text{CO}$ ,  $\text{N}_2$ , and  $\text{NH}_3$  and the most important atoms are Na and K.

We determine when water condenses by comparing the water ice condensation curve (the total pressure at which the partial pressure of water is at saturation) with the object’s T/P profile. For pressures lower than that near the associated intercept, we deplete the vapor phase through the expected rainout and embed an absorbing/scattering water-ice cloud with a thickness of one pressure-scale-height in the region above. Note that the total gas pressures at which the partial pressure of water is at the triple-point pressure of water are generally higher than the intercept pressures we find. Hence, the water gas to water ice (solid) transition is the more relevant. Note also that the optical properties of water ice and water droplets are not very different. The ice particles are assumed to be spherical and their modal particle radii are derived using the theory of Cooper et al. (2003). They vary in size from  $\sim 20 \mu\text{m}$  (higher- $g$ /lower- $T_{\text{eff}}$ ) to  $\sim 150 \mu\text{m}$  (lower- $g$ /higher- $T_{\text{eff}}$ ) and we assume that the particle size is independent of altitude. A canonical super-saturation factor (Cooper et al. 2003; Ackermann and Marley 2001) of 0.01 (1.0%) is used. Curiously, with such large particles and such a small super-saturation, the absorptive opacity of our baseline water-ice

clouds, when they do form, is not large. In fact, the consequences for the emergent spectrum of the associated drying of the upper atmosphere, and the corresponding diminution of the water vapor abundance there, are comparable to the effects on the spectrum of the clouds themselves. Without an external flux source, and the scattering of that flux back into space by clouds, water-ice clouds seem to have only a secondary influence on the spectra of the coolest isolated brown dwarfs.

We use the constantly-updated opacity database described in Burrows et al. (1997,2001,2002). This includes Rayleigh scattering, Collision-Induced Absorption (CIA) for  $\text{H}_2$  (Borysow and Frommhold 1990; Borysow, Jørgensen, and Zheng 1997), and T/P-dependent absorptive opacities from  $0.3 \mu\text{m}$  to  $300 \mu\text{m}$  for  $\text{H}_2\text{O}$ ,  $\text{CH}_4$ ,  $\text{CO}$ , and  $\text{NH}_3$ . The opacities of the alkali metal atoms are taken from Burrows, Marley, and Sharp (2000), which are similar in the line cores and near wings to those found in Burrows and Volobuyev (2003). The opacities are tabulated in T/ $\rho$ /frequency space using the abundances derived for a solar-metallicity elemental abundance pattern (Anders and Grevesse 1989; Grevesse and Sauval 1998; Allende-Prieto, Lambert, and Asplund 2002). During the TLUSTY iterations, the opacity at any thermodynamic point and for any wavelength is obtained by interpolation. The absorptive opacities for the ice particles are derived using Mie theory with the frequency-dependent spectrum of the complex index of refraction of water ice. Ammonia clouds form in the upper atmospheres of the coldest exemplars of the late brown dwarf family ( $T_{\text{eff}} \leq 160 \text{ K}$ ; §4). Nevertheless, since the scattering of incident radiation that gives them their true importance in the Jovian context is absent, we ignore them here.

### 3. Model Set

We have chosen for this study a set of models with the masses and ages given in Table 1. Also shown in Table 1 are the corresponding gravities and  $T_{\text{eff}}$ s. These models span an effective temperature range from  $\sim 800 \text{ K}$  to  $\sim 150 \text{ K}$  that allows us to probe the realm between the known T dwarfs and the known Jovian planets. To establish the mapping between mass/age pairs and the  $T_{\text{eff}}/g$  pairs that are needed for atmospheric calculations, we use the evolutionary models of Burrows et al. (1997). While this procedure does not ensure that the atmospheres we calculate are fully consistent with those evolutionary tracks, the errors are not large.

Figure 1 depicts evolutionary trajectories and isochrones in  $T_{\text{eff}}/g$  space for models in the realm beyond the T dwarfs. The depicted isochrones span the range from  $10^7$  to  $5 \times 10^9$  years and the masses cover the range from  $0.5 M_J$  to  $25 M_J$ . The large dots denote the models found in Table 1 for which we have calculated spectra and atmospheres. For contrast, the approximate region in which the currently known T dwarfs reside is also shown. In addition, we provide the demarcation lines that separate (in a rough sense) the cloud-free models from those with water clouds and ammonia clouds. The clouds form to the left of the corresponding condensation lines. Figure 1 emphasizes the transitional and as-yet-unstudied character of this family of objects. It also provides at a glance a global summary of family properties. Figure 2 is a companion figure to Fig. 1, but shows iso- $T_{\text{eff}}$  lines in mass/age space. For a given mass, Fig. 2 allows one to determine

the evolution of  $T_{\text{eff}}$  and at what age a given  $T_{\text{eff}}$  is achieved. It also makes easy the determination of the combination of mass and age for which clouds form, as well as the minimum mass for which a given  $T_{\text{eff}}$  is reached after approximately the galactic disk's or the sun's age ( $\sim 10^{10}$  and  $\sim 4.6 \times 10^9$  years, respectively). For instance, Fig. 2 shows that it takes  $\sim 200$  Myr for a  $2-M_J$  object to reach a  $T_{\text{eff}}$  of 400 K, that it takes the same object 1 Gyr to reach a  $T_{\text{eff}}$  of  $\sim 250$  K, and that in the age of the solar system a  $2-M_J$  object can reach the  $\text{NH}_3$  condensation line. Similarly, Fig. 2 indicates that a  $10-M_J$  object takes  $\sim 1$  Gyr to reach a  $T_{\text{eff}}$  of  $\sim 400$  K, and that it has water-ice clouds in its upper atmosphere. Figures 1 and 2 are, therefore, useful maps of the model domain to which the reader may want often to return.

To calculate absolute fluxes at 10 parsecs one needs the radius of the object. We determine this for each model in Table 1 by using a fit to the results of Burrows et al. (1997) that works reasonably well below  $\sim 25 M_J$  and after deuterium burning has ended:

$$R = 0.94 \left( \frac{g}{10^5 \text{ cm s}^{-2}} \right)^{-0.18} \left( \frac{T_{\text{eff}}}{1000 \text{ K}} \right)^{0.11} R_J, \quad (1)$$

where  $R_J$  is Jupiter's radius ( $\sim 7.15 \times 10^9$  cm).

#### 4. Temperature-Pressure Profiles

Shown in Fig. 3 are representative temperature-pressure profiles at 300 Myr (blue) for models with masses of 1, 2, 5, 7, and  $10 M_J$  and at 5 Gyr (red) for models with masses of 2, 5, 7, 10, 15, 20, and  $25 M_J$ . Superposed are the water ice and ammonia condensation lines at solar metallicity. The radiative-convective boundary pressures are near 0.1-1.0 bars for the lowest-mass, oldest models and are near 10-30 bars for the youngest, most massive models. At a given temperature, lower-mass objects have higher pressures (at a given age). Similarly, an object with a given mass evolves to higher and higher pressures at a given temperature. This trend is made clear in Fig. 4, in which the evolving T/P profiles for  $1-M_J$  and  $5-M_J$  models are depicted, and is not unexpected (Marley et al. 1996,2002; Burrows et al. 1997). Note that Fig. 4 implies that a  $5-M_J$  object takes  $\sim 300$  Myr to form water clouds, but that a  $1-M_J$  object takes only  $\sim 100$  Myr. After  $\sim 1$  Gyr, a  $1-M_J$  object forms ammonia clouds, signature features of Jupiter itself. These numbers echo the information also found in Fig. 2.

The appearance of a water-ice cloud manifests itself in Figs. 3 and 4 by the kink in the T/P profile near the intercept with the associated condensation line. Generally, the higher the intercept of the T/P profile with the condensation line (the lower the intercept pressure) the smaller the droplet size (Cooper et al. 2003). Note that after an age of  $\sim 300$  Myr a  $7-M_J$  object is expected to form water clouds high up in its atmosphere and that after  $\sim 5$  Gyr even a  $25-M_J$  object will do so. The higher the atmospheric pressure at which the cloud forms the greater the column thickness of the cloud. This results in a stronger cloud signature for the lower-mass models than for the higher-mass models. However, given the generally large ice particle sizes derived with the Cooper

et al. (2003) model, the low assumed supersaturation (§2), the tendency for larger particle radii to form for larger intercept pressures, and the modest to low imaginary part of the index of refraction for pure water ice, the effect of water clouds in our model set is not large. This translates into a small cloud effect on the corresponding flux spectra (§6).

Figure 5 portrays the evolution of the T/P profiles for  $10-M_J$  and  $20-M_J$  objects. This figure is provided to show, among other things, the position of the forsterite ( $Mg_2SiO_4$ ) condensation line relative to that of water ice.  $Mg_2SiO_4$  clouds exist in these brown dwarfs, but at significantly higher pressures and temperatures and are, therefore, buried from view. Hence, unlike in L dwarfs, such clouds have very little effect on the emergent spectra of the coolest brown dwarfs that are the subject of this paper.

Finally, the high pressures achieved at low temperatures for the lowest mass, oldest objects shown in Figs. 3, 4, and 5 suggest that the CIA (pressure-induced) opacity of  $H_2$  might for them be important. This is indeed the case at longer wavelengths and is discussed in §6. We mention this because CIA opacity is yet another characteristic signature of the Jovian planets in our own solar system and to emphasize yet again that our cold brown dwarf model suite is a bridge between the realms of the planets and the “stars.”

## 5. SIRTF and JWST Point-Source Sensitivities

Before we present and describe our model spectra, we discuss the anticipated point-source sensitivities of the instruments on board the SIRTf and JWST space telescopes. SIRTf has a 0.84-meter aperture and is to be launched in mid-April of 2003. JWST is planned to have a collecting area of  $\sim 25$  square meters over a segmented 6-meter diameter mirror and is to be launched at the beginning of the next decade. While SIRTf is the last of the “Great Observatories,” and will view the sky with unprecedented infrared sensitivity, JWST will in turn provide a two- to four-order-of-magnitude gain in sensitivity through much of the mid-infrared up to 27 microns. While their fields of view are limited and missions like WISE (formerly NGSS; Wright et al. 2001) are more appropriate for large-area surveys, the extreme sensitivity of both SIRTf and JWST will bring the coolest brown dwarfs and isolated giant planets into the realm of detectability and study.

SIRTf/IRAC has four channels centered at  $3.63 \mu m$ ,  $4.53 \mu m$ ,  $5.78 \mu m$ , and  $8.0 \mu m$  that are thought to have  $5-\sigma$  point-source sensitivities for 200-second integrations of  $\sim 2.5$ ,  $\sim 4.5$ ,  $\sim 15.5$ , and  $\sim 25.0$  microJanskys, respectively. HST/NICMOS achieves a bit better than one microJansky sensitivity at  $2.2 \mu m$ , but does not extend as far into the near IR. The short-wavelength, low-spectral resolution module (“Short-low”) of SIRTf/IRS extends from  $\sim 5.0 \mu m$  to  $\sim 14.0 \mu m$  and has a  $5-\sigma$  point-source sensitivity for a 500-second integration of  $\sim 100$  microJanskys. The other three modules on IRS cover other mid-IR wavelength regimes at either low- or high-spectral resolution, but will have smaller brown dwarf detection ranges. The  $\sim 20.5 \mu m$  to  $\sim 26 \mu m$  channel on SIRTf/MIPS is the most relevant channel on MIPS for brown dwarf studies and has a suggested  $1-\sigma$  point-source

sensitivity at  $\sim 24 \mu\text{m}$  of  $\sim 70$  microJanskys. This is  $\sim 1000$  times better in imaging mode than for the pioneering IRAS. All these SIRTf sensitivities are derived from various SIRTf web pages and are pre-launch estimates (<http://sirtf.caltech.edu>). Furthermore, for all three SIRTf instruments, one can estimate the point-source sensitivities for different values of the signal-to-noise and integration times. However, these signals-to-noise and integration times are the nominal combinations for each instrument and the quoted sensitivities serve to guide our assessment of SIRTf’s capabilities for cool brown dwarf studies in advance of real on-orbit calibrations and measurements.

The capabilities of JWST are even more provisional, but the design goals for its instruments are impressive (<http://ngst.gsfc.nasa.gov>). JWST/NIRCam is to span  $\sim 0.6 \mu\text{m}$  to  $\sim 5.0 \mu\text{m}$  in various wavelength channels/filters, though the final design has not been frozen. The seven so-called “B” filters have widths of 0.5–1.0 microns centered at  $\sim 0.71$ ,  $\sim 1.1$ ,  $\sim 1.5$ ,  $\sim 2.0$ ,  $\sim 2.7$ ,  $\sim 3.6$ , and  $\sim 4.4$  microns and are expected to have  $5\text{-}\sigma$  point-source sensitivities in imaging mode, for an assumed exposure time of  $5 \times 10^4$  seconds, of  $\sim 1.6$ ,  $\sim 0.95$ ,  $\sim 1.0$ ,  $\sim 1.2$ ,  $\sim 0.95$ ,  $\sim 1.05$ , and  $\sim 1.5$  nanoJanskys (nJ), respectively. In addition, a set of so-called “I” filters, with about half to one quarter the spectral width of the B filters, and sensitivities comparable to that of the B filters, are available in the 1.5–5.0  $\mu\text{m}$  region. Furthermore, JWST/NIRCam may have a tunable filter to examine selected spectral regions beyond 2.5  $\mu\text{m}$  at a resolution ( $R = \lambda/\Delta\lambda$ ) of  $\sim 100$ , though at the time of this writing the availability of such a capability remained uncertain. Hence, with JWST/NIRCam we enter the world of *nano*Jansky sensitivity. This is greater than one hundred times more sensitive than HST/NICMOS at 2.2  $\mu\text{m}$  and enables one to probe deeply in space, as well as broadly in wavelength. JWST/MIRI spans the mid-IR wavelength range from  $\sim 5.0 \mu\text{m}$  to  $\sim 27.0 \mu\text{m}$  and will have in imaging mode a  $10\text{-}\sigma$  point-source sensitivity for a  $10^4$ -second integration of from  $\sim 63$  nJ at the shortest wavelength to  $\sim 10$  microJanskys at the longest. This is orders of magnitude more sensitive than any previous mid-IR telescope in imaging mode. (In spectral mode with an  $R$  near 1000, JWST/MIRI will be  $\sim 100$  times less sensitive than in imaging mode.) Given the importance of the mid-IR for understanding those brown dwarfs that may exist in relative abundance at  $T_{\text{eff}}$ s cooler than those of the currently known T dwarfs, MIRI provides what is perhaps a transformational capability. As with SIRTf, the quoted JWST sensitivities are taken from the associated web pages and, hence, should be considered tentative.

We now turn to a discussion of the spectra, spectral evolution, defining features, systematics, and diagnostics for the cool brown dwarf models listed in Table 1 and embedded in Figs. 1 and 2. On each of Figs. 6 to 11 in §6, we plot for the SIRTf (red) and JWST (blue) instruments the broadband sensitivities we have summarized in this section.

## 6. Cool Brown Dwarf Spectra

Using the numerical tools and data referred to in §2, and the mapping between  $T_{\text{eff}}/g$  and mass/age found in Table 1, we have generated a grid of spectral and atmospheric models for cool brown dwarfs that reside in the low- $T_{\text{eff}}$  sector of  $T_{\text{eff}}/g$  space (Fig. 1). Some of the associated

T/P profiles were given in Figs. 3, 4, and 5. In Figs. 6 to 11, we plot theoretical flux spectra ( $F_\nu$ , in milliJanskys) from the optical to  $30 \mu\text{m}$  at a distance of 10 parsecs. These figures constitute the major results of our paper. For comparison, superposed on each figure are the estimated point-source sensitivities of the instruments on board SIRTf and JWST (§5). In addition, included at the top of Figs. 8 through 11 are the rough positions of the major atmospheric absorption features. (The full model set is available from the first author upon request.)

Figures 6 and 7 portray the mass dependence of a cool brown dwarf’s flux spectrum at 10 parsecs for ages of one and five Gyr, respectively. The model masses are 25, 20, 15, 10, 7, 5, 2, and  $1 M_J$ . The top panels depict the most massive four, while the bottom panels depict the least massive four (three for Fig. 7). Together they show the monotonic diminution of flux with object mass at a given age that parallels the associated decrease in  $T_{\text{eff}}$  with mass (from  $\sim 800$  K to  $\sim 130$  K) seen in Table 1 and Fig. 2.

Figures 6 through 11 show the peaks due to enhanced flux through the water vapor absorption bands that define the classical terrestrial photometric bands ( $Z$ ,  $J$ ,  $H$ ,  $K$ , and  $M$ ) and that have come to characterize brown dwarfs since the discovery of Gliese 229B (Oppenheimer et al. 1995; Marley et al. 1996). For the more massive models, the near-IR fluxes are significantly above black-body values. At  $T_{\text{eff}} \sim 800$  K, the  $25-M_J/1\text{-Gyr}$  model shown in Fig. 6 could represent the known late T dwarfs, but all other models in this model set are “later” and, hence, represent as yet undetected objects.

Apart from the distinctive water troughs, generic features are the hump at 4-5 microns ( $M$  band), the broad hump near 10 microns, the methane features at  $2.2 \mu\text{m}$ ,  $3.3 \mu\text{m}$ ,  $7.8 \mu\text{m}$ , and in the optical (particularly at  $0.89 \mu\text{m}$ ), the ammonia features at  $\sim 1.5 \mu\text{m}$ ,  $\sim 1.95 \mu\text{m}$ ,  $\sim 2.95 \mu\text{m}$ , and  $\sim 10.5 \mu\text{m}$ , and the Na-D and K I resonance lines at  $0.589 \mu\text{m}$  and  $0.77 \mu\text{m}$ , respectively. However, as Figs. 6-11 indicate, the strengths of each of these features are functions of mass and age.

For lower masses or greater ages, the centroid of the  $M$  band hump shifts from  $\sim 4.0 \mu\text{m}$  to  $\sim 5.0 \mu\text{m}$ . In part, this is due to the swift decrease with  $T_{\text{eff}}$  at the shorter wavelengths of the Wien tail. Even after the collapse of the flux in the optical and near-IR after  $\sim 1$  Gyr for masses below  $5 M_J$  or after  $\sim 5$  Gyr for masses below  $10 M_J$ , the  $M$  band flux persists as a characteristic marker and will be SIRTf’s best target. Moreover, IRAC’s filters are well-positioned for this task. As one would expect, the relative importance of the mid-IR fluxes, in particular between 10 and 30 microns, grows with decreasing mass and increasing age. Since this spectral region is near the linear Rayleigh-Jeans tail, fluxes here persist despite decreases in  $T_{\text{eff}}$  from  $\sim 800$  K to  $\sim 130$  K. Figure 11 depicts this clearly for the older  $2-M_J$  models. The rough periodicity in flux beyond  $10 \mu\text{m}$  is due predominantly to the presence of pure rotational bands of water and, for cooler models, methane as well. For the coldest models depicted in Figs. 6, 7, and 11, this behavior subsides, but is replaced with long-period undulations due to CIA absorption by  $\text{H}_2$ . Such a signature is characteristic of Jovian planets and is expected for low-T, high-P atmospheres. Its appearance marks yet another



transition, seen first in this model set for the old  $5-M_J$  and middle-aged  $2-M_J$  objects, between T-dwarf-like and “planet”-like behavior. As Figs. 6-11 imply, SIRTf/MIPS should be able to detect at 10 parsecs the  $\sim 24\text{-}\mu\text{m}$  flux of objects more massive than  $2\text{-}4 M_J$  at age 1 Gyr or more massive than  $10 M_J$  at 5 Gyr.

Methane forms at low temperatures and high pressures and makes its presence felt in older and less massive objects. Hence, its features at  $0.89 \mu\text{m}$ ,  $2.2 \mu\text{m}$ ,  $3.3 \mu\text{m}$ , and  $7.8 \mu\text{m}$  deepen with age and decreasing mass. An example of such strengthening at  $7.8 \mu\text{m}$  and  $2.2 \mu\text{m}$  can be seen in Fig. 10 by comparing the 100-Myr and 5-Gyr models with a mass of  $5 M_J$ . Clear indications of the strengthening of the methane absorption feature at  $0.89 \mu\text{m}$  with decreasing mass can be seen in the upper panel of Fig. 7. This trend is accompanied by a corresponding weakening of the Cs I feature on top of it. However, due to its presence in the *I* band at relatively short wavelengths, the methane feature at  $0.89 \mu\text{m}$  may be difficult to detect for all but the youngest and/or most massive models. The actual strength of the  $7.8\text{-}\mu\text{m}$  feature depends on the T/P profile in the upper layers of the atmosphere, which in turn might be affected by ambient UV (disfavored for free-floating brown dwarfs) or processes that could create a stratosphere and a temperature inversion. Hence, the filling in or reshaping of the  $7.8\text{-}\mu\text{m}$  feature might signal the presence of a stratosphere. Such a temperature inversion could also affect the depths of the water troughs.

As can be seen by comparing the top panels of Figs. 8-11, the alkali metal features at  $0.589 \mu\text{m}$  and  $0.77 \mu\text{m}$  diminish in strength with decreasing mass and increasing age. These features are signatures of the known T dwarfs (Burrows, Marley, and Sharp 2000; Burrows et al. 2002; Tsuji, Ohnaka, and Aoki 1999), so their decay signals a gradual transformation away from standard T-dwarf behavior. For the  $10\text{-}M_J$  model older than 1 Gyr and the  $2\text{-}M_J$  model older than 100 Myr, these alkali resonance features cease to be primary signatures. This happens near a  $T_{\text{eff}}$  of 450 K.

Ammonia makes an appearance at even lower temperatures than methane and due to the relatively high abundance of nitrogen its absorption features are generally strong, particularly for the cool objects in our model set. For the higher  $T_{\text{eff}}$ s in the mid-T-dwarf range, ammonia may have been seen, but is weak (Saumon et al. 2000). Figs. 10 and 11 evince strong ammonia features in the upper panels at  $\sim 1.5 \mu\text{m}$ ,  $\sim 1.95 \mu\text{m}$ , and  $\sim 2.95 \mu\text{m}$  and in Figs. 8-11 in the lower panels at  $\sim 10.5 \mu\text{m}$ . As Figs. 6-11 imply, the Short-low module on SIRTf/IRS should be able to study the  $10.5\text{-}\mu\text{m}$  ammonia feature. Even for the  $25\text{-}M_J/1\text{Gyr}$  model, the  $\sim 10.5 \mu\text{m}$  feature is prominent. For the more massive objects ( $10\text{-}25 M_J$ ), the strength of the  $10.5\text{-}\mu\text{m}$  feature increases with age. For the lowest mass objects ( $2\text{-}7 M_J$ ), the strength of the  $10.5\text{-}\mu\text{m}$  ammonia feature actually decreases with age, even though the strengths of the other ammonia lines increase. As the more massive objects age, their atmospheric pressures increase, shifting the  $\text{N}_2/\text{NH}_3$  equilibrium towards  $\text{NH}_3$ . For the less massive models, pressured-induced absorption by  $\text{H}_2$  grows with increasing atmospheric pressure (Fig. 3-4) and partially flattens an otherwise strengthening  $10.5\text{-}\mu\text{m}$  ammonia feature.

Below  $T_{\text{eff}}$ s of  $\sim 160$  K, Figs. 1 and 2 demonstrate that ammonia clouds form. However, given that we are studying isolated objects that have no reflected component (unlike Jupiter and Saturn),

and given that realistic supersaturations are only  $\sim 1\%$ , we have determined that ammonia clouds do not appreciably affect the emergent spectra. As a consequence, we ignore them in the three relevant models (Fig. 1).

As with the known T and L dwarfs, water vapor absorptions dominate and sculpt the flux spectra of the cooler brown dwarfs and these features generally deepen with increasing age and decreasing mass. The latter trend is in part a consequence of the increase with decreasing gravity of the column depth of water above the (roughly-defined) photosphere. At  $T_{\text{eff}}$ s below  $\sim 400\text{-}500$  K (Figs. 1-5), water condenses in brown dwarf atmospheres. The appearance of such water-ice clouds constitutes yet another milestone along the bridge from the known T dwarfs to the giant planets. Associated with cloud formation is the depletion of water vapor above the tops of the water cloud, with the concomitant decrease at altitude in the gas-phase abundance of water. Within  $\sim 100$  Myr, water clouds form in the atmosphere of an isolated  $1-M_J$  object and within  $\sim 5$  Gyr they form in the atmosphere of a  $25-M_J$  object. In fact, approximately two-thirds of the models listed in Table 1 incorporate water-ice clouds. However, at supersaturations of 1% and for particle sizes above 10 microns (§2-§4; Cooper et al. 2003), such clouds (and the corresponding water vapor depletions above them) only marginally affect the calculated emergent spectra. Even though we see in Figs. 3-5 the associated kinks in the T/P profiles, these do not translate into a qualitative change in the emergent spectra at any wavelength. For wavelengths longward of 1 micron, the cloudy spectra differ from the no-cloud spectra by at most a few tens of percent. For a representative  $2-M_J$  model at 300 Myr ( $T_{\text{eff}} \sim 280$  K), if we increase the supersaturation factor by a factor of ten from 1% to 10%, the flux at 5 microns decreases by approximately a factor of two, while the flux from 10 to 30 microns increases by on average  $\sim 50\%$ . These are not large changes, given the many orders of magnitude covered by the fluxes in Figs. 6-11.

The prominence of water features provides a guide to the optimal placement of NIRCcam filters for the detection and characterization of brown dwarfs. For example, the water feature near  $0.93 \mu\text{m}$  is missed by the B filters, while those features at  $\sim 1.4$  and  $\sim 1.8 \mu\text{m}$  are not centered on the respective adjacent filters and, hence, are diluted by the adjoining continuum. The I filters on NIRCcam would partially overcome these limitations. Even so, as Fig. 12 shows, the broadband fluxes in the NIRCcam filters provide useful diagnostics of the differences among brown dwarfs and extrasolar giant planets (here expressed as mass at a given age), with particular sensitivity to the large flux differences between the  $5\text{-}\mu\text{m}$  window and the region shortward. A tunable filter could provide even greater diagnostic capability by permitting in and around the  $5\text{-}\mu\text{m}$  window a spectral resolution near 100 to more definitively characterize the effective temperature and, hence, the mass of detected objects (for a given age and composition). Nevertheless, Fig. 7 indicates that at 10 parsecs even a  $7-M_J$  object at 5 Gyr should easily be detected in imaging mode in the *J* and *H* bands. In the *M* band, a  $2-M_J$  object could be seen by NIRCcam out to  $\sim 100$  parsecs. Furthermore, a  $25-M_J$  object at 5 Gyr and a distance of 1000 parsecs should be detectable by NIRCcam in a number of its current broadband filters.

Figure 13 shows predicted spectra of a  $20-M_J / 5\text{-Gyr}$  model in the mid-infrared for the SIRTf/IRS

and JWST/MIRI instruments. To generate the SIRTf/IRS curve in Fig. 13, we multiplied the theoretical spectra by the IRS response curves for the entire wavelength range, not just the 5-14  $\mu\text{m}$  of the “Short-low” module. The IRS spectral resolution has been assumed to be 100, while that of JWST/MIRI is  $\sim 1000$ . We find that the IRS spectra are useful at 10 parsecs only for the warmer brown dwarfs ( $> 15 M_J$ ), but for these brown dwarfs even at this modest spectral resolution one can clearly identify the various dominant molecular bands.

In its broadband detection (imaging) mode, JWST/MIRI will be  $\sim 100$  times more capable than SIRTf from  $\sim 5 \mu\text{m}$  to  $\sim 27 \mu\text{m}$  (§5). Since the mid-IR is one of the spectral regions of choice for the study of the coolest brown dwarfs, MIRI will assume for their characterization a role of dramatic importance. At wavelengths longward of  $15\text{-}\mu\text{m}$ , MIRI will be able to detect objects 10 parsecs away down to  $2 M_J$  or lower. In addition, it could detect an object just 10 times the mass of Jupiter with an age of 5 Gyr out to a distance of one kiloparsec. Furthermore, JWST/MIRI provides 10 times better spectral resolution than SIRTf/IRS for objects down to  $10 M_J$ .

Figs. 6 through 13 collectively summarize the flux spectra and evolution of the cool brown dwarfs yet to be discovered, as well as the extraordinary capabilities of the various instruments on board both SIRTf and JWST for the diagnosis and characterization of their atmospheres. These figures highlight the prominent molecular features of  $\text{H}_2\text{O}$ ,  $\text{CH}_4$ ,  $\text{NH}_3$ , in particular, that are pivotal in the evolution of the differences between the coolest brown dwarfs and the known T dwarfs, most of which are at higher  $T_{\text{eff}}$ s and gravities. The latest known T dwarf has been typed a T8 (Burgasser et al. 2000a), but its effective temperature is near 750-800 K (Geballe et al. 2001; Burrows et al. 2002). This does not leave much room for the expansion of the T dwarf subtypes to the lower  $T_{\text{eff}}$ s and masses discussed in this paper, and suggests that yet another spectroscopic class beyond the T dwarfs might be called for. Many of the spectral trends described in this paper are gradual, but the near disappearance of the alkali features below  $T_{\text{eff}} = 500$  K, the onset of water cloud formation below  $T_{\text{eff}} = 400\text{-}500$  K, the collapse below  $\sim 350$  K of the optical and near-IR fluxes relative to those longward of  $\sim 5 \mu\text{m}$ , and the growing strengths of the  $\text{NH}_3$  features all suggest physical reasons for such a new class. Figure 14 depicts isochrones from 100 Myr to 5 Gyr on the  $M_J$  versus  $J - K$  color-magnitude diagram and demonstrates that the blueward trend in  $J - K$  that so typifies the T dwarfs stops and turns around (Marley et al. 2002; Stephens, Marley, and Noll 2001) between effective temperatures of 300 and 400 K. This is predominantly due not to the appearance of water clouds, but to the long-expected collapse of flux on the Wien tail. Note that the  $T_{\text{eff}}$  at which the  $J - K$  color turns around is not the same for all the isochrones. This is because the colors are not functions of just  $T_{\text{eff}}$ , but of gravity as well. The decrease in  $T_{\text{eff}}$ , that for the T dwarfs squeezes the  $K$ -band flux more than the  $J$ -band flux, finally does to  $J - K$  what people had expected such a decrease to do before the discovery of T dwarfs, i.e., redden the color. We remind the reader that unlike M dwarfs, the  $J - K$  colors of T dwarfs actually get bluer with decreasing  $T_{\text{eff}}$  (for a given surface gravity). This may be counterintuitive, but it is a result of the increasing role of methane and  $\text{H}_2$  collision-induced absorption with decreasing temperature, as well as the positive slope of the opacity/wavelength curve of water and its gradual steepening

with decreasing temperature.

Were it not for the extremely low fluxes at such low  $T_{\text{eff}}$ s shortward of 4 microns, we might have suggested the use of this turnaround to mark the beginning of a new spectroscopic class. Moreover, clearly the optical can not be used and with the diminishing utility of the near infrared as  $T_{\text{eff}}$  drops, that leaves the mid-IR longward of  $\sim 4 \mu\text{m}$  as the most logical part of the spectrum with which to characterize a new spectroscopic class. As is usual, this will be determined observationally, and it might be done arbitrarily to limit the growth of the T sequence. Nevertheless, we observe that the  $T_{\text{eff}}$  region between 300 K and 500 K witnesses a few physical transitions that might provide a natural break between “stellar” types.

## 7. Conclusions

We have generated a new set of brown dwarf spectral models that incorporate state-of-the-art opacities and the effects of water clouds. Our focus has been on the low- $T_{\text{eff}}$  branch of the brown dwarf tree beyond the known T dwarfs. To this end, we have investigated the  $T_{\text{eff}}$  range from  $\sim 800$  K to  $\sim 130$  K and the low-mass range from 25 to 1  $M_{\text{J}}$ . As Fig. 1 indicates, this is mostly unexplored territory. Our calculations have been done to provide a theoretical foundation for the new brown dwarf studies that will be enabled by the launch of SIRTF and the eventual launch of JWST, as well as for the ongoing ground-based searches for the coolest substellar objects. We provide spectra from  $\sim 0.4 \mu\text{m}$  to  $30 \mu\text{m}$ , investigate the dependence on age and mass of the strengths of the  $\text{H}_2\text{O}$ ,  $\text{CH}_4$ , and  $\text{NH}_3$  molecular features, address the formation and effect of water clouds, and compare the calculated fluxes with the suggested sensitivities of the instruments on board SIRTF and JWST. From the latter, detection ranges can be derived, which for JWST can exceed a kiloparsec. We find that the blueward trend in near-infrared colors so characteristic of the T dwarfs stops near a  $T_{\text{eff}}$  of 300-400 K and we identify a few natural physical transitions in the low- $T_{\text{eff}}$  realm which might justify the eventual designation of at least one new spectroscopic type after the T dwarfs. These include the formation of water clouds ( $\sim 400$ -500 K), the strengthening of ammonia bands, the eventual collapse in the optical, the shift in the position of the  $M$  band peak, the turnaround of the  $J - K$  color, the near disappearance of the strong Na-D and K I resonance lines ( $\sim 500$  K), and the increasing importance with decreasing  $T_{\text{eff}}$  of the mid-IR longward of  $4 \mu\text{m}$ . For these cooler objects, the mid-infrared assumes a new and central importance and first MIPS and IRS on SIRTF, then MIRI on JWST, are destined to play pivotal roles in their future characterization and study.

Finally, the formation of ammonia clouds below  $\sim 160$  K suggests yet another natural breakpoint, and a second new “stellar” class. Therefore, there are reasons to anticipate that perhaps two naturally defined, yet uncharted, spectral types reside beyond the T dwarfs at lower  $T_{\text{eff}}$ s.

The current filter set for JWST/NIRCam from  $0.6$  to  $5.0 \mu\text{m}$  is good, but not yet fully optimized for cool brown dwarf detection. Placing filters on the derived spectral peaks and troughs (robustly

defined by the water bands) would improve its already good performance for substellar research. In any case, our theoretical spectra are meant to bridge the gap between the known T dwarfs and those cool, low-mass free-floating brown dwarfs with progressively more planetary features which may inhabit the galaxy in interesting, but as yet unknown, numbers.

The authors thank Ivan Hubeny, Bill Hubbard, John Milsom, Christopher Sharp, Jim Liebert, Curtis Cooper, and Jonathan Fortney for fruitful conversations and help during the course of this work, as well as NASA for its financial support via grants NAG5-10760, NAG5-10629, and NAG5-12459.

## REFERENCES

- Ackermann, A. and Marley, M.S. 2001, *ApJ*, 556, 872
- Allende-Prieto, C., Lambert, D.L., and Asplund, M. 2002, *ApJ*, 573, L137
- Anders, E. and Grevesse, N. 1989, *Geochim. Cosmochim. Acta*, 53, 197
- Bessell, M.S., and Brett, J. M. 1988, *PASP*, 100, 1134
- Borysow, A. and Frommhold, L. 1990, *ApJ*, 348, L41
- Borysow, A., Jørgensen, U.G., and Zheng, C. 1997, *A&A*, 324, 185
- Burgasser, A.J., et al. 1999, *ApJ*, 522, L65
- Burgasser, A.J., et al. 2000a, *ApJ*, 531, L57
- Burgasser, A.J., Kirkpatrick, J. D., Reid, I. N., Liebert, J., Gizis, J. E., & Brown, M. E. 2000b, *AJ*, 120, 473
- Burgasser, A.J., et al. 2000c, *AJ*, 120, 1100
- Burrows, A., Marley M., Hubbard, W.B. Lunine, J.I., Guillot, T., Saumon, D. Freedman, R., Sudarsky, D. and Sharp, C.M. 1997, *ApJ*, 491, 856
- Burrows, A. and Sharp, C.M. 1999, *ApJ*, 512, 843
- Burrows, A., Marley, M. S., and Sharp, C. M. 2000, *ApJ*, 531, 438
- Burrows, A., Hubbard, W.B., Lunine, J.I., and Liebert, J. 2001, *Rev. Mod. Phys.*, 73, 719
- Burrows, A., Burgasser, A.J., Kirkpatrick, J. D., Liebert, J., Milsom, J.A., Sudarsky, D., and Hubeny, I. 2002, *ApJ*, 573, 394
- Burrows, A. and Volobuyev, M. 2003, *ApJ*, 583, 985
- Cooper, C.S., Sudarsky, D., Milsom, J.A., Lunine, J.I., & Burrows, A. 2003, *ApJ*, 586, 1320
- Delfosse, X., Tinney, C.G., Forveille, T., Epchtein, N., Bertin, E., Borsenberger, J., Copet, E., De Batz, B., Fouqué, P., Kimeswenger, S., Le Bertre, T., Lacombe, F., Rouan, D., and Tiphène, D. 1997, *Astron. Astrophys.*, 327, L25

- Geballe, T.R., Saumon, D., Leggett, S.K., Knapp, G.R., Marley, M.S., and Lodders, K. 2001, *ApJ*, 556, 373
- Grevesse, N., Sauval, A.J. 1998, *Space Sci. Rev.*, 85, 161
- Hubeny, I. 1988, *Computer Physics Comm.*, 52, 103
- Hubeny, I. 1992, in *The Atmospheres of Early-Type Stars*, ed. U. Heber & C. J. Jeffery, Lecture Notes in Phys. 401, (Berlin: Springer), 377
- Hubeny, I. and Lanz, T. 1995, *ApJ*, 439, 875
- Kirkpatrick, J.D., Reid, I.N., Liebert, J., Cutri, R.M., Nelson, B., Beichman, C.A., Dahn, C.C., Monet, D.G., Gizis, J., and Skrutskie, M.F. 1999, *ApJ*, 519, 802
- Kirkpatrick, J. D., Reid, I. N., Liebert, J., Gizis, J. E., Burgasser, A. J., Monet, D. G., Dahn, C. C., Nelson, B., & Williams, R. J. 2000, *AJ*, 120, 447
- Marley, M.S., Saumon, D., Guillot, T., Freedman, R.S., Hubbard, W.B., Burrows, A. & Lunine, J.I. 1996, *Science*, 272, 1919
- Marley, M.S., Seager, S., Saumon, D., Lodders, K., Ackerman, A.S., Freedman, R., and Fan, X. 2002, *ApJ*, 568, 335
- Martín, E. L., Delfosse, X., Basri, G., Goldman, B., Forveille, T., & Zapatero Osorio, M. R. 1999, *AJ*, 118, 2466
- Mather, J.C. and Stockman, H.S. 2000, *Proc. SPIE*, 4013, p. 2-16 (JWST/NGST)
- Oppenheimer, B.R., Kulkarni, S.R., Matthews, K., and Nakajima, T. 1995, *Science*, 270, 1478
- Reid, I.N. 1994, *Astrophys. and Space Sci.*, 217, 57
- Saumon, D., Chabrier, G., and Van Horn, H.M. 1995, *ApJS*, 99, 713
- Saumon, D., Geballe, T.R., Leggett, S.K., Marley, M.S., Freedman, R.S., Lodders, K., Fegley, B., and Sengupta, S.K. 2000, *ApJ*, 541, 374
- Stephens, D., Marley, M.S., and Noll, K. 2001, in *Ultracool Dwarfs: New Spectral Types L and T* (Springer: Berlin, Heidelberg), edited by H.R.A. Jones and I.A. Steele, p. 183
- Stiening, R., Skrutskie, M.F., and Capps, R. 1995, *Bull. A.A.S.*, 187, 7508 (2MASS)
- Strauss, M.A., et al. 1999, *ApJ*, 522, L61
- Tsuji, T., Ohnaka, K., and Aoki, W. 1999, *ApJ*, 520, L119
- Werner, M.W. and Fanson, J.L., *Proc. SPIE*, 2475, p. 418-427 (SIRTF)
- Wright, E. and the NGSS team 2001, *Bull. A.A.S.*, 198, 407

Table 1. Cool Brown Dwarf Model Grid

$M/M_J$	$\log_{10} t (yr)$	$T_{\text{eff}} (K)$	$\log_{10} g (\text{cm s}^{-2})$
1	8.0	290	3.23
	8.5	216	3.27
	9.0	159	3.32
2	8.0	386	3.53
	8.5	283	3.57
	9.0	208	3.60
	9.5	149	3.63
	9.7	134	3.64
5	8.0	588	3.92
	8.5	426	3.96
	9.0	312	3.99
	9.5	225	4.02
	9.7	197	4.03
7	8.0	703	4.07
	8.5	507	4.12
	9.0	369	4.15
	9.5	267	4.18
	9.7	234	4.19
10	8.0	859	4.24
	8.5	620	4.29
	9.0	447	4.32
	9.5	325	4.35
	9.7	284	4.36
15	9.0	593	4.52
	9.5	414	4.56
	9.7	359	4.57
20	9.0	686	4.66
	9.5	483	4.71
	9.7	421	4.72
25	9.0	797	4.80
	9.5	555	4.83
	9.7	483	4.85

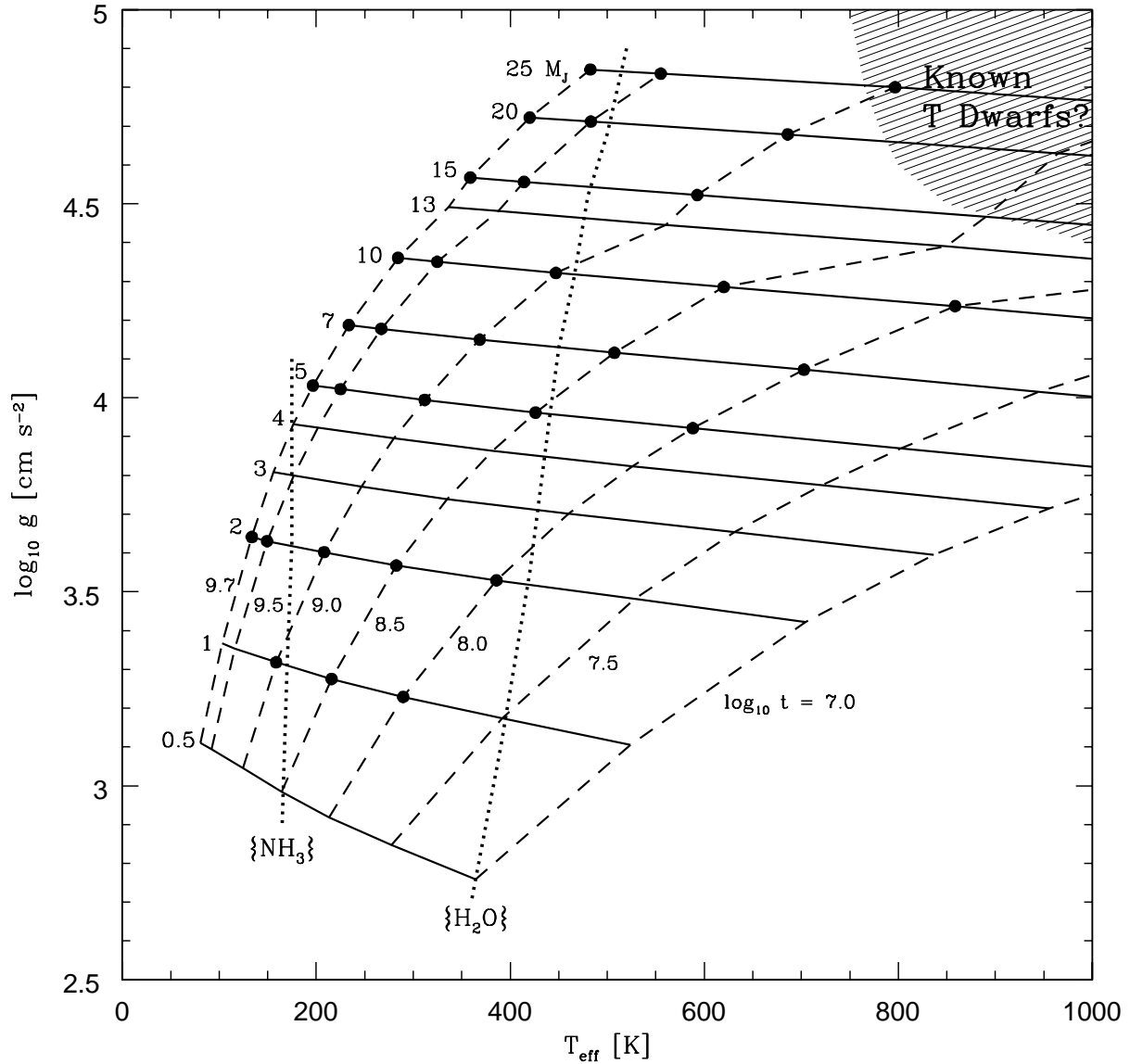


Fig. 1.— Gravity versus effective temperature for a range of brown dwarf masses (0.5 to 25  $M_J$ ) and ages (10 Myr to 5 Gyr). The solid curves depict evolutionary tracks, while the dashed curves are isochrones. The large dots denote the object parameters for which we calculate spectra and atmospheres for this paper. The approximate condensation curves for water and ammonia are plotted as dotted lines. For objects to the left of these lines the corresponding condensate will form in the atmosphere. As indicated, water is expected to condense in the atmospheres of a sizable subset of these models, while ammonia is expected to condense for only the lowest mass, oldest objects. The hatched region in the top right identifies in approximate fashion where the currently known T dwarfs reside. As seen, they occupy only a small fraction of the depicted phase space.



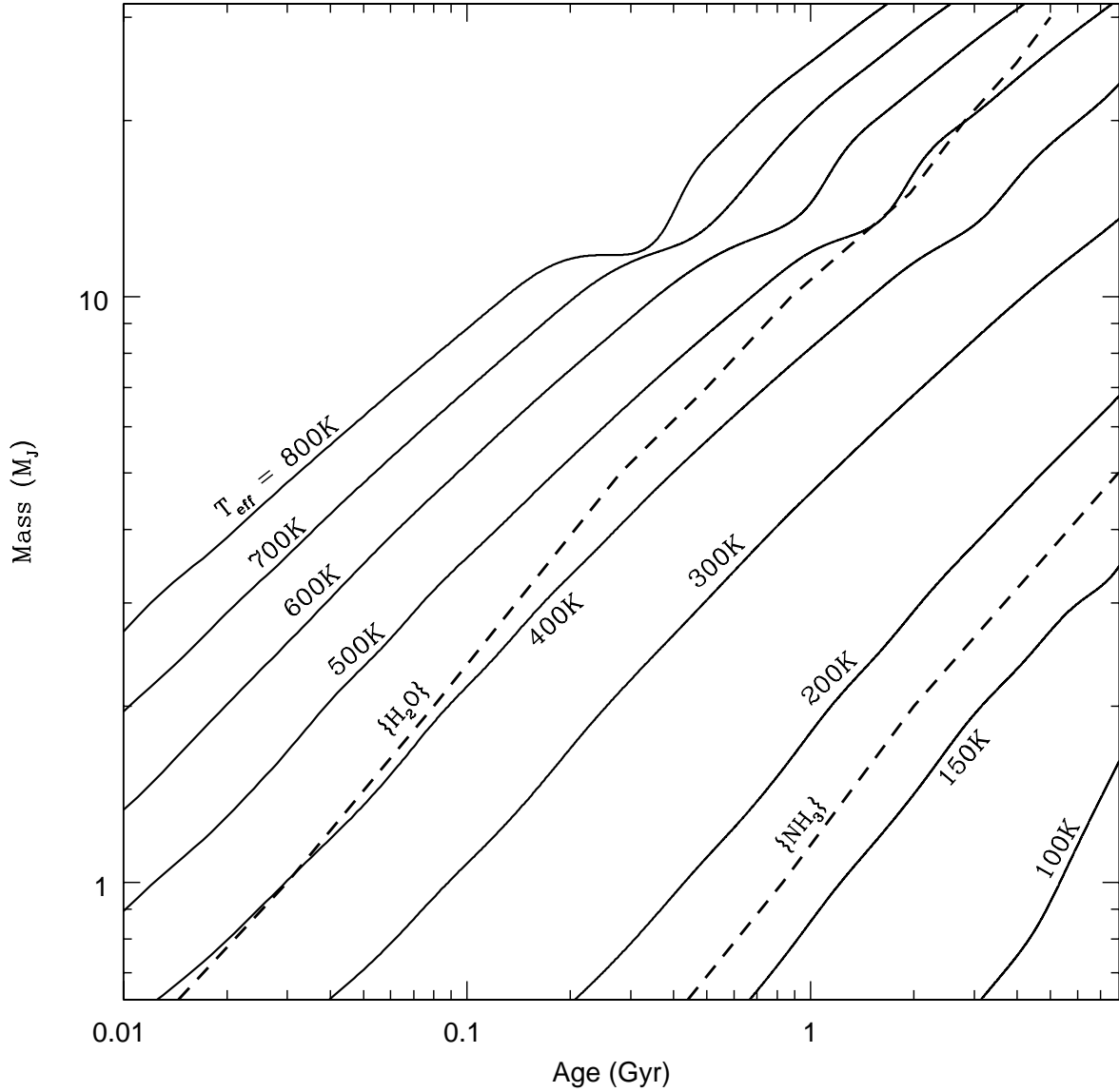


Fig. 2.— Brown dwarf mass (in  $M_J$ ) versus age (in Gyr) for a variety of effective temperatures. At a constant mass, incrementing the age (i.e., reading horizontally from left to right) reveals the decline in  $T_{\text{eff}}$  with time. Additionally, along such a trajectory, the condensation curves for water and ammonia indicate the ages at which the condensation of these species first ensues in the outer atmosphere. The kink near  $\sim 13 M_J$  is a consequence of deuterium burning.

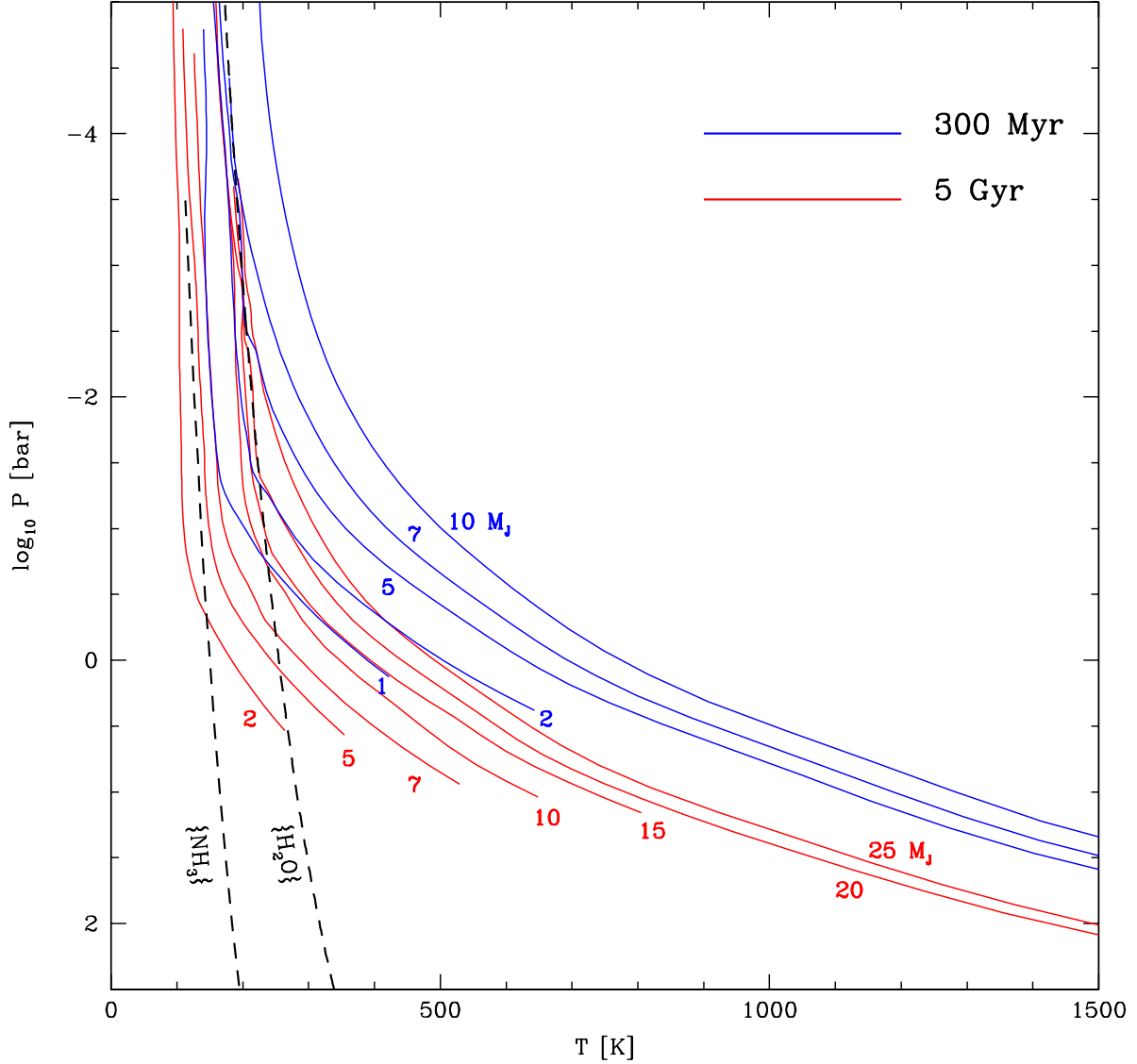


Fig. 3.— Atmospheric temperature ( $T$ , in Kelvin) versus pressure ( $P$ , in bars) for a selection of lower-mass brown dwarfs, both young (blue, 300 million years) and old (red, 5 billion years). The ordinate goes from high pressures at the bottom to low pressures at the top. Also shown are the condensation curves for water and ammonia (dashed curves). The presence of water clouds is expected to be important in low-mass and/or old objects. Ammonia clouds are likely to be relevant only in the lowest-mass, oldest brown dwarfs.

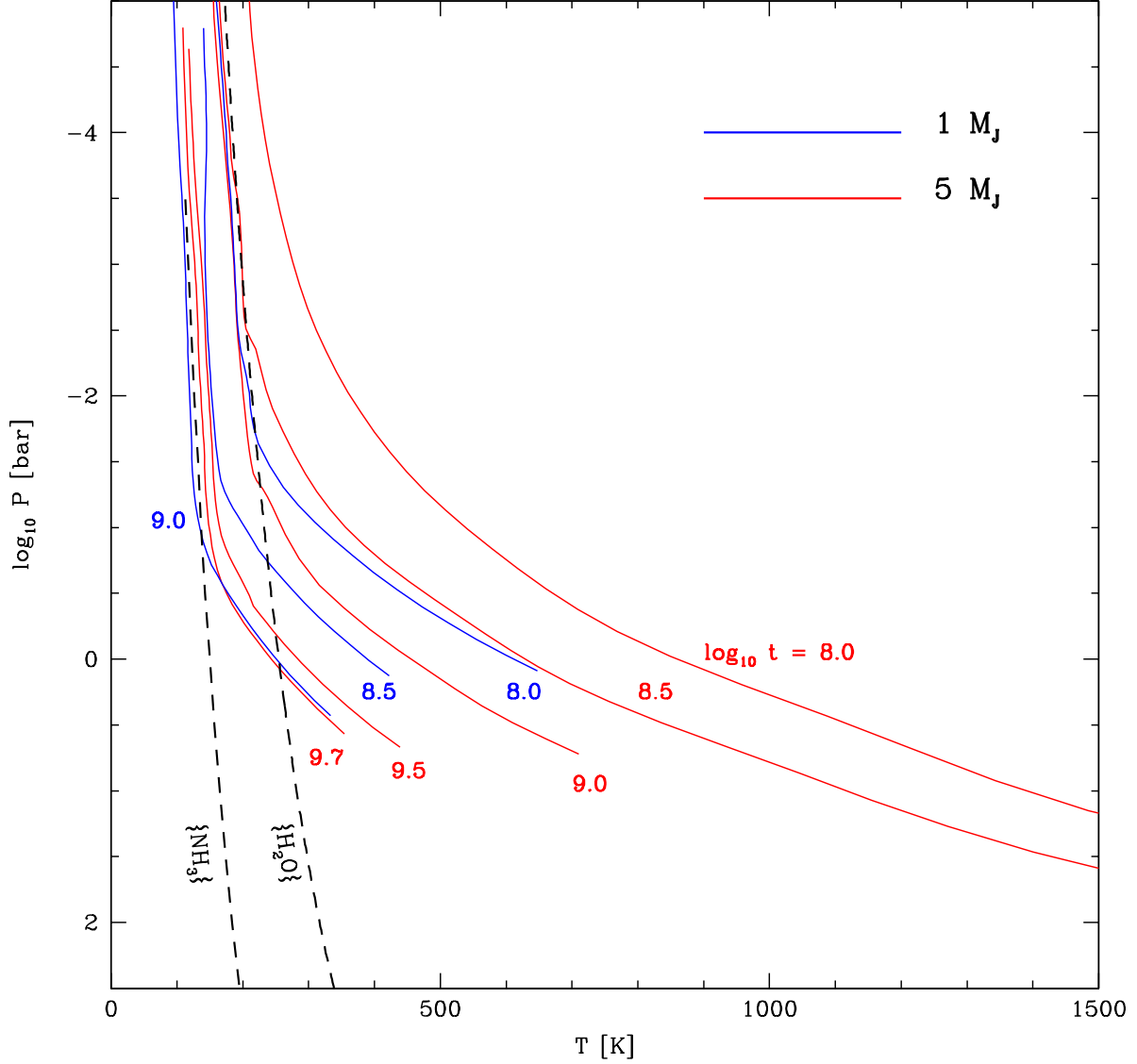


Fig. 4.— Atmospheric temperature ( $T$ , in Kelvin) versus pressure ( $P$ , in bars) profiles for models with 1 (blue) and 5 (red) Jupiter masses and for a variety of ages (in years). Also shown are the condensation curves for water and ammonia (dashed curves). The atmospheres of  $\sim 2/3$  of the objects in our model set form some condensed water; an isolated  $1-M_J$  object is also expected to contain condensed ammonia after an age of 1 billion years.

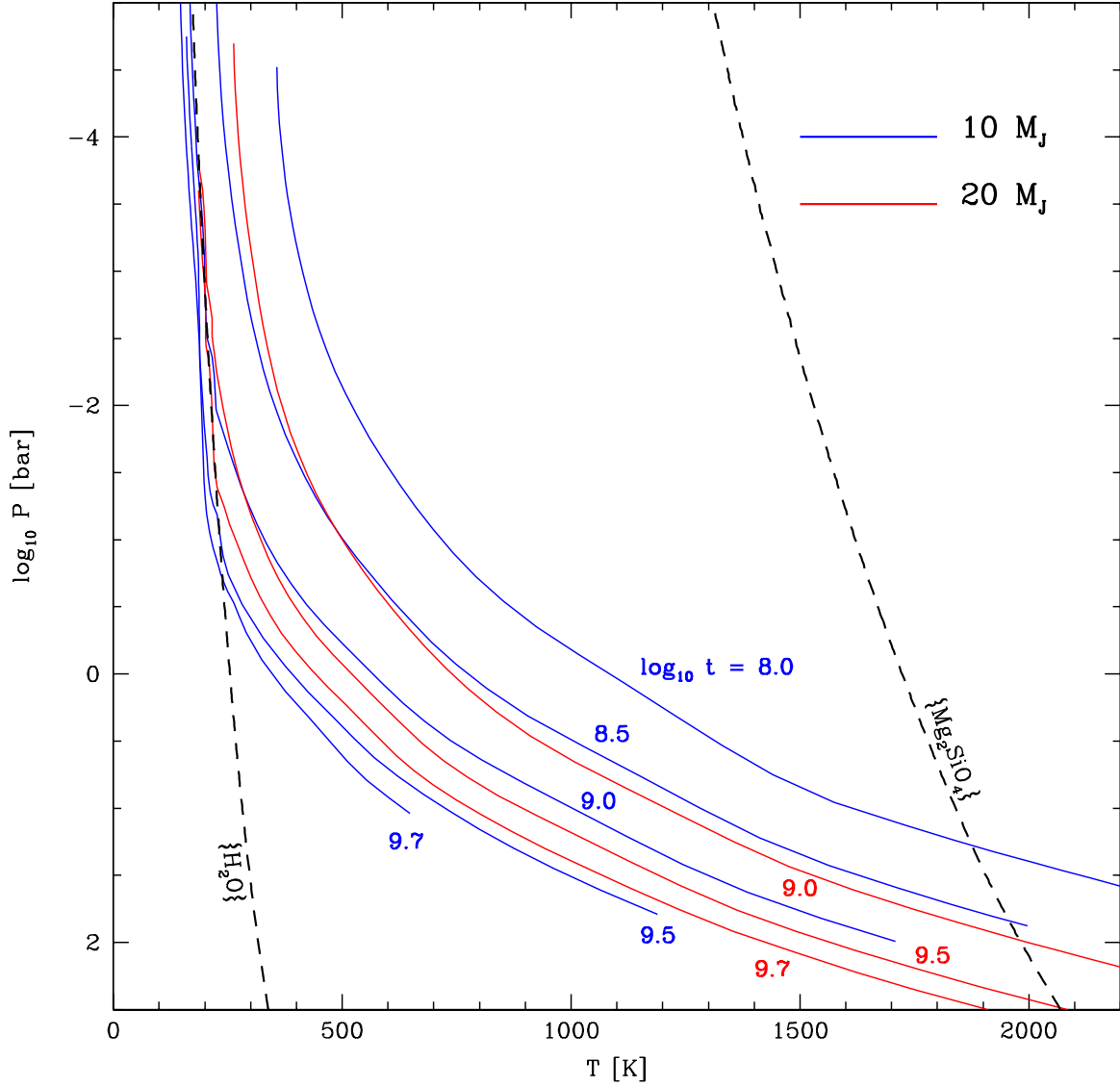


Fig. 5.— T/P profiles, as in Figs. 3 and 4, but for  $10 M_J$  and  $20 M_J$  models and for a variety of ages (in years). Also shown are the condensation curves (dashed) for water and forsterite, a representative silicate. The oldest  $20 M_J$  objects are expected to contain some condensed water in their outer atmospheres. Silicate layers will be buried deeply, typically at pressures near  $\sim 100$  bars.

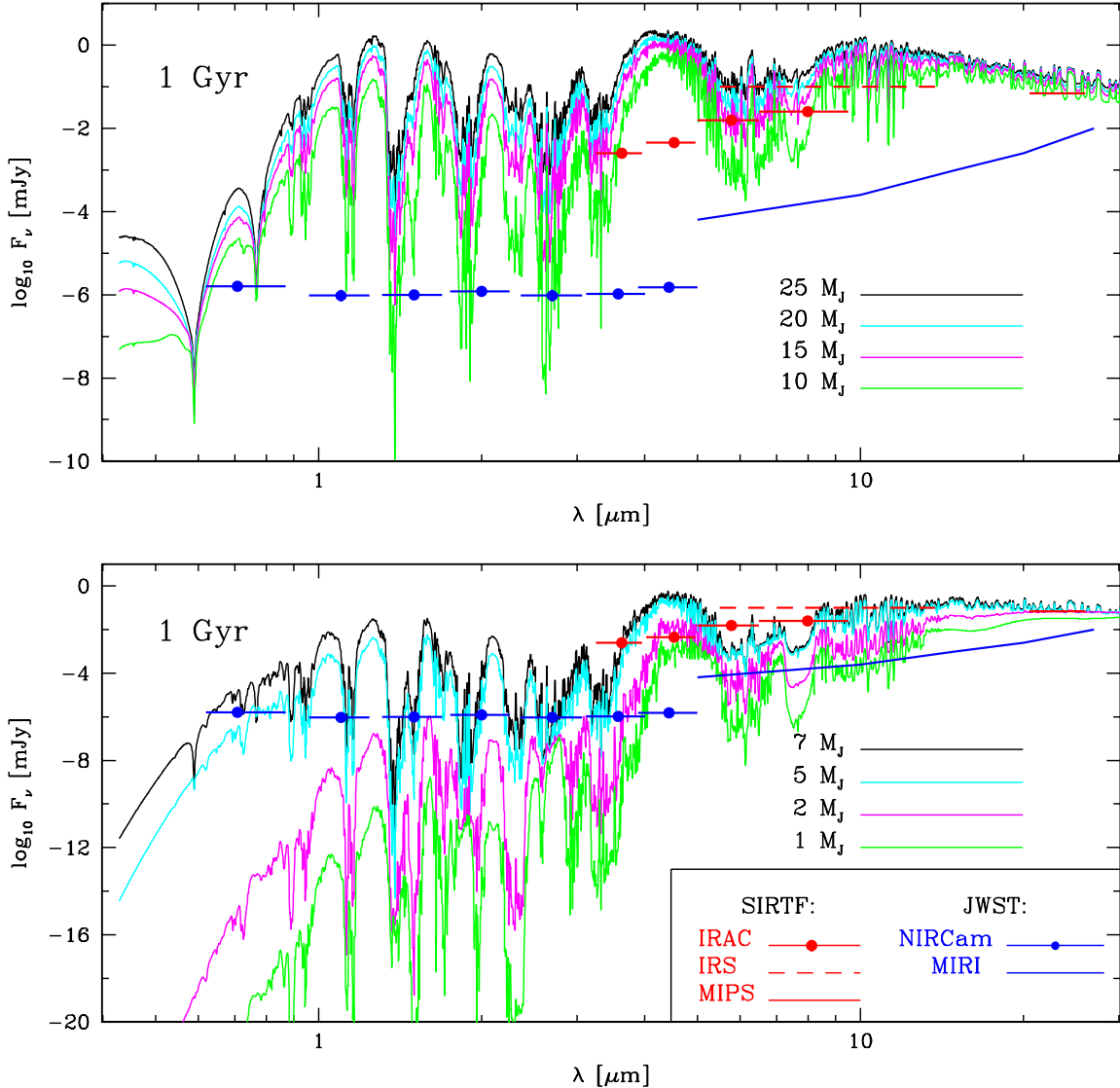


Fig. 6.— Spectra ( $F_\nu$ , in milliJanskys) versus wavelength (in microns) for a range of brown dwarf masses at an age of 1 Gyr and a distance of 10 pc. The top panel is for masses of 25, 20, 15, and 10  $M_J$  and the bottom panel is for masses of 7, 5, 2, and 1  $M_J$ . Note that the ordinate scales are different. Flux densities are plotted for wavelengths from  $\sim 0.4$  to 30  $\mu\text{m}$ . Superposed are the approximate point-source sensitivities for instruments on SIRTTF (red) and JWST (blue) (see §5). All sensitivities are for imaging mode, except for those of SIRTTF/IRS, which are for spectral mode. The SIRTTF/IRAC sensitivities for its channels 1 (3.63  $\mu\text{m}$ ), 2 (4.53  $\mu\text{m}$ ), 3 (5.78  $\mu\text{m}$ ), and 4 (8.0  $\mu\text{m}$ ) are 5- $\sigma$  and are for an exposure time of 200 seconds. The 5- $\sigma$  “Short-low” SIRTTF/IRS sensitivities (dashed) from 5.0 to 14  $\mu\text{m}$  are for an exposure time of 500 seconds. The SIRTTF/MIPS 1- $\sigma$  sensitivities (dotted) are for wavelengths from 20.5 to 26  $\mu\text{m}$  and an exposure time of 200 seconds. The JWST/NIRCam sensitivities for its B1 (0.71  $\mu\text{m}$ ), B2 (1.1  $\mu\text{m}$ ), B3 (1.5  $\mu\text{m}$ ), B4 (2.0  $\mu\text{m}$ ), B5 (2.7  $\mu\text{m}$ ), B6 (3.57  $\mu\text{m}$ ), and B7 (4.44  $\mu\text{m}$ ) bands are 5- $\sigma$  and assume an exposure time of  $5 \times 10^4$  seconds. The JWST/MIRI sensitivity curve from 5.0 to 27  $\mu\text{m}$  is 10- $\sigma$  and assumes an exposure time of  $10^4$  seconds. See text for discussion.

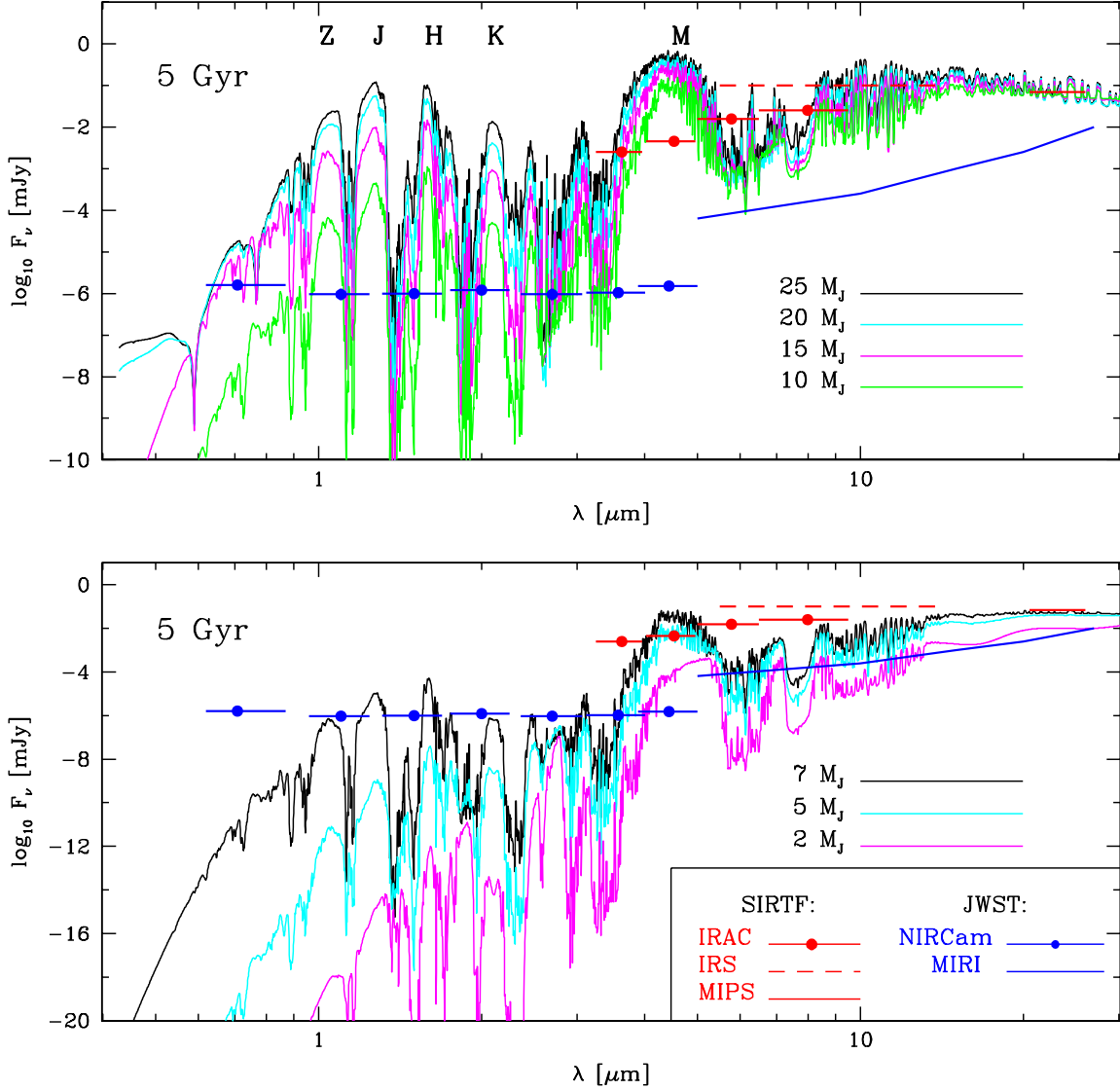


Fig. 7.— Spectra ( $F_\nu$ , in milliJanskys) for a range of brown dwarf masses at an age of 5 billion years and a distance of 10 pc. Flux densities are plotted from  $\sim 0.4$  to  $30 \mu\text{m}$ . The top panel is for masses of 25, 20, 15, and 10  $M_J$  and the bottom panel is for masses of 7, 5, and 2  $M_J$ . The positions of the Z, J, H, K, and M photometric bands are indicated in the top panel. Superposed are the suggested point-source sensitivities for instruments on SIRTTF (red) and JWST (blue) that are described in §5 and in the caption to Fig. 6.

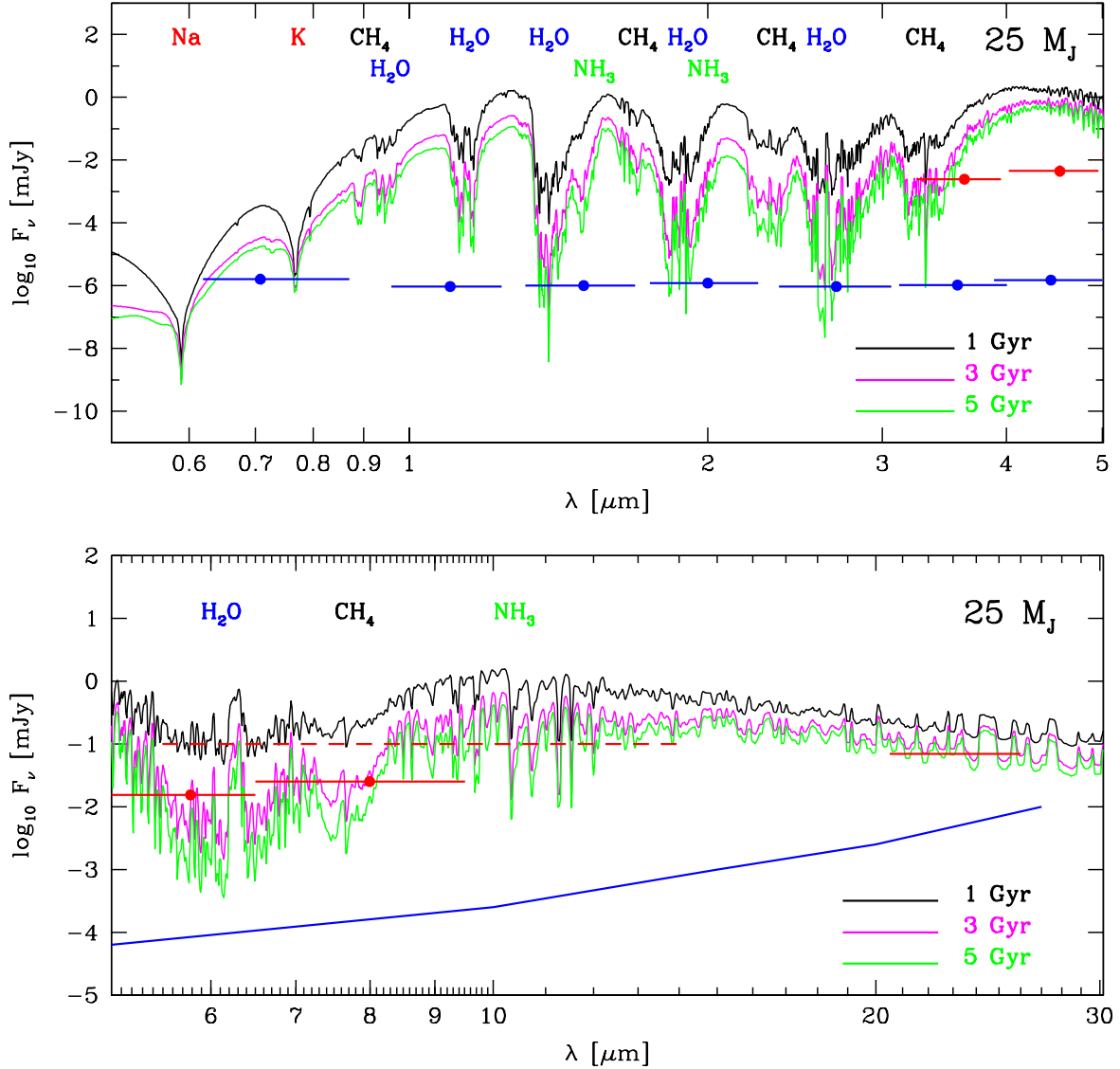


Fig. 8.— Spectra ( $F_\nu$  in milliJanskys versus wavelength in microns) of 25- $M_J$  brown dwarfs at 1, 3, and 5 billion years. As in Figure 6, SIRTf and JWST detector sensitivities are also plotted (see Figure 6 for legend). The top panel is from 0.5  $\mu\text{m}$  to 5  $\mu\text{m}$  and the bottom panel is from 5  $\mu\text{m}$  to 30  $\mu\text{m}$ . Gaseous water absorption features and the pressure-broadened sodium and potassium resonance lines remain strong over this range of ages, while methane and ammonia features strengthen with age. The wavelength positions of various of the molecular and atomic features are depicted for reference on this and subsequent figures. See text for details.

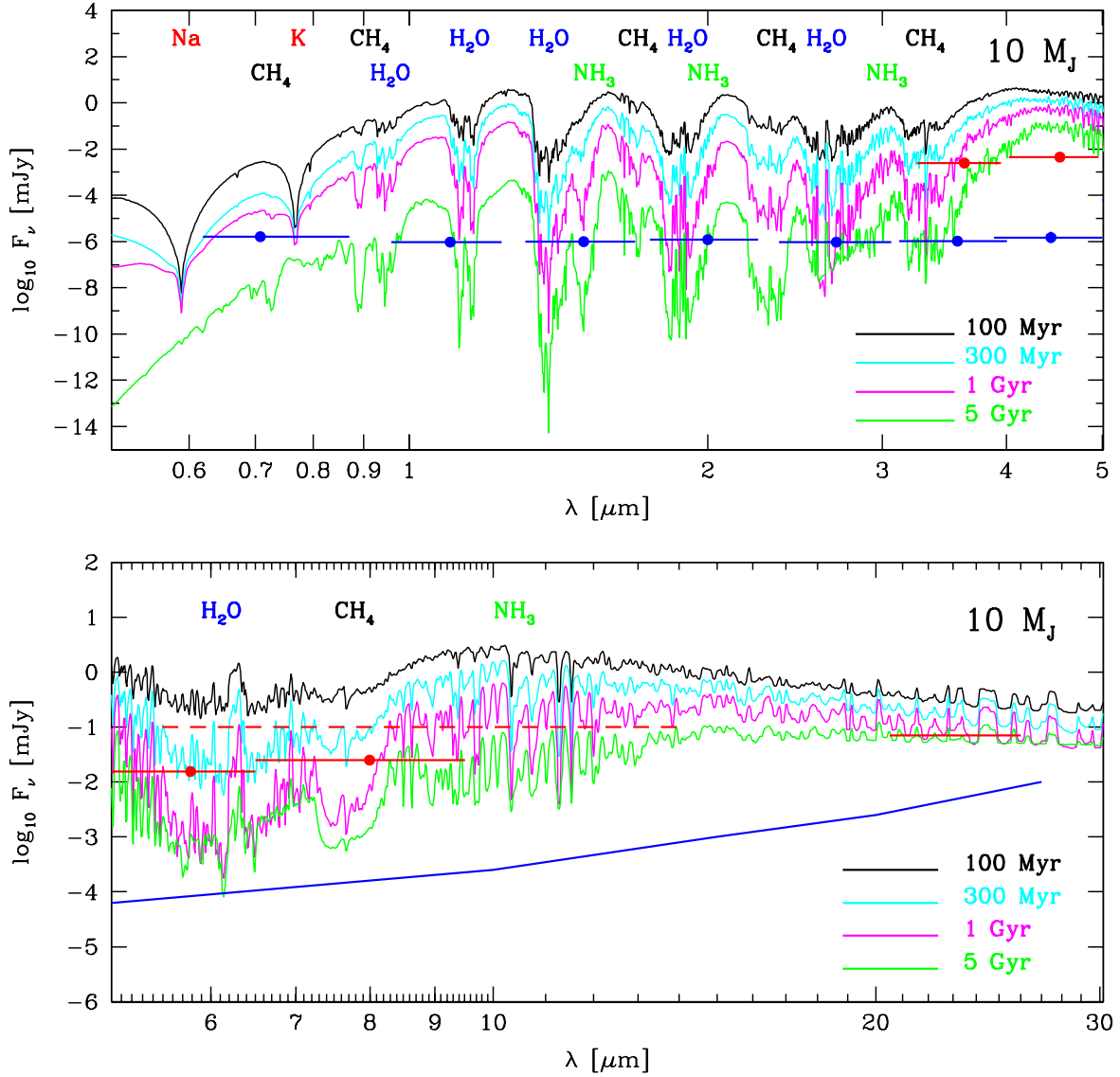


Fig. 9.— Similar to Fig. 8, but for  $10-M_J$  brown dwarfs at  $10^8$ ,  $3 \times 10^8$ ,  $10^9$ , and  $5 \times 10^9$  years. As in Figure 6, SIRTf and JWST detector sensitivities are plotted (see Figure 6 for legend). The top panel is from  $0.5 \mu\text{m}$  to  $5 \mu\text{m}$  and the bottom panel is from  $5 \mu\text{m}$  to  $30 \mu\text{m}$ . Methane and ammonia absorption features strengthen with age, as the alkali lines wane.



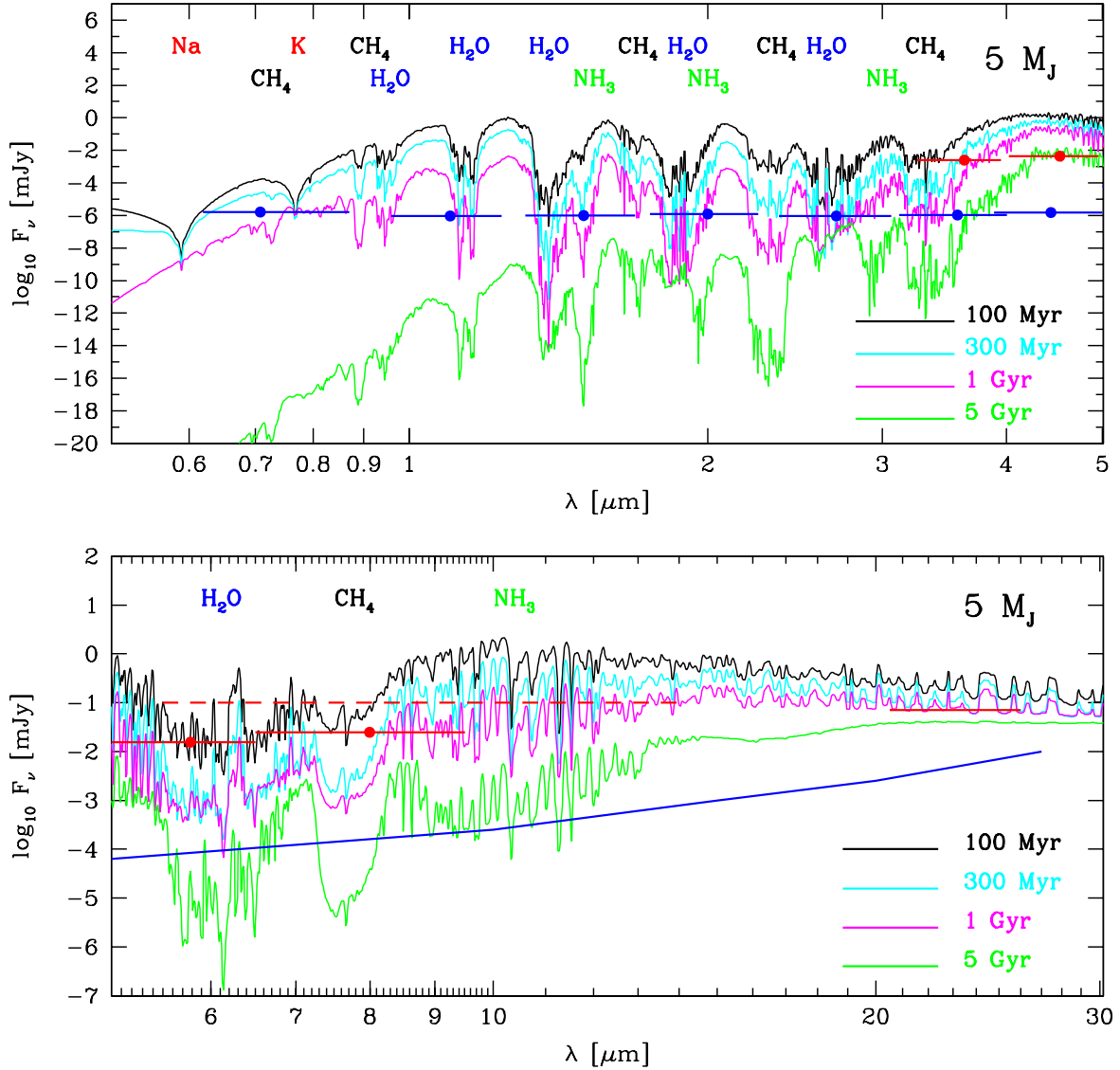


Fig. 10.— Similar to Fig. 8, but for 5- $M_J$  brown dwarfs at  $10^8$ ,  $3 \times 10^8$ ,  $10^9$ , and  $5 \times 10^9$  years. Flux densities are in milliJanskys and the wavelengths are from 0.5  $\mu\text{m}$  to 5  $\mu\text{m}$  in the top panel and from 5  $\mu\text{m}$  to 30  $\mu\text{m}$  in the bottom panel. As in Figure 6, SIRTIF and JWST detector sensitivities are plotted (see Figure 6 for legend). Methane and ammonia absorption features strengthen with age.

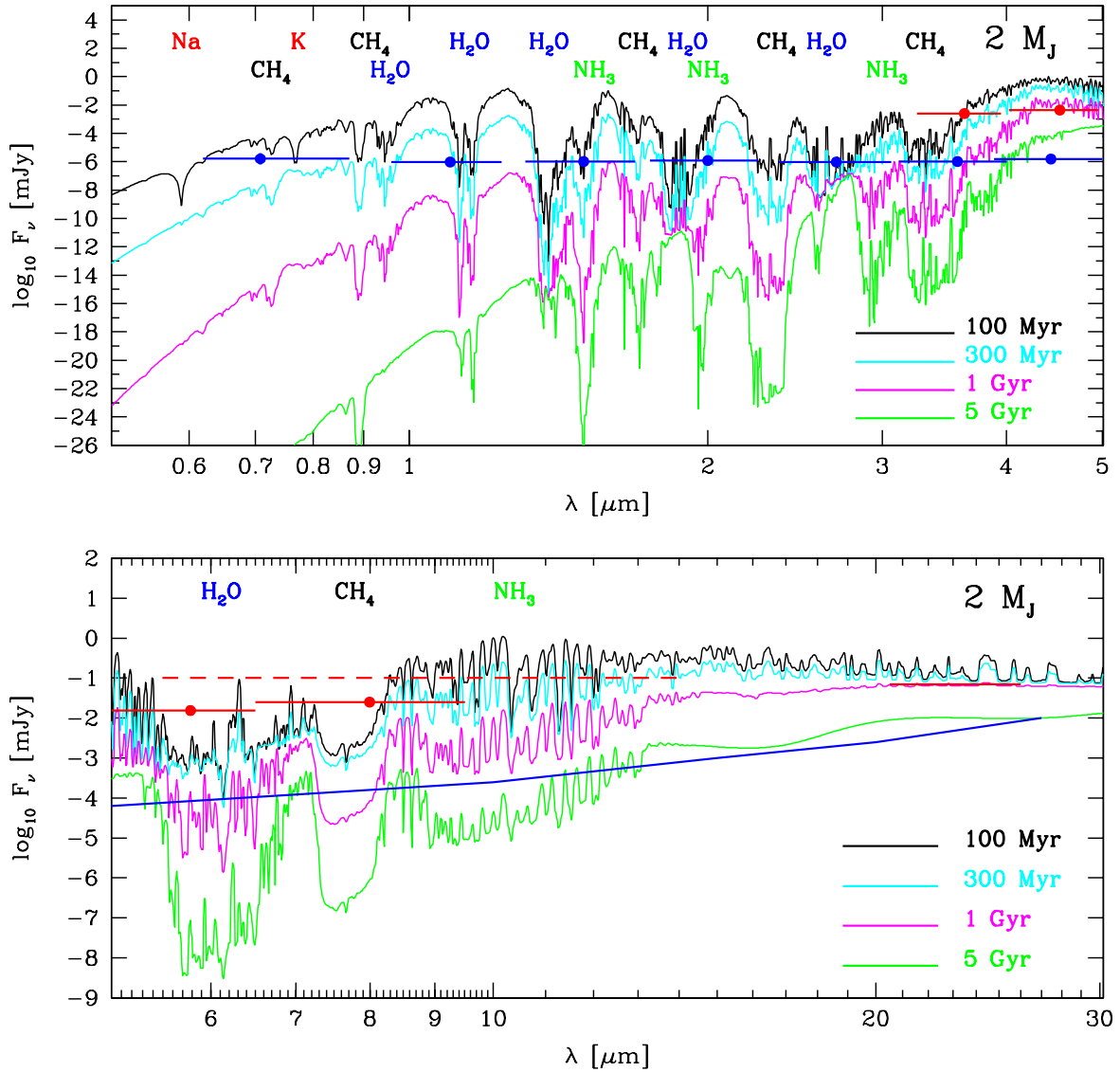


Fig. 11.— Similar to Figs. 8 through 10, but for  $2-M_J$  brown dwarfs at  $10^8$ ,  $3 \times 10^8$ ,  $10^9$ , and  $5 \times 10^9$  years. As in Figure 6, SIRTf and JWST detector sensitivities are plotted (see Figure 6 for legend). The top panel is from  $0.5 \mu\text{m}$  to  $5 \mu\text{m}$  and the bottom panel is from  $5 \mu\text{m}$  to  $30 \mu\text{m}$ . Methane absorption features are strong over this full range of ages, while the ammonia features strengthen with age. The sodium and potassium resonance lines are prominent in only the youngest objects.

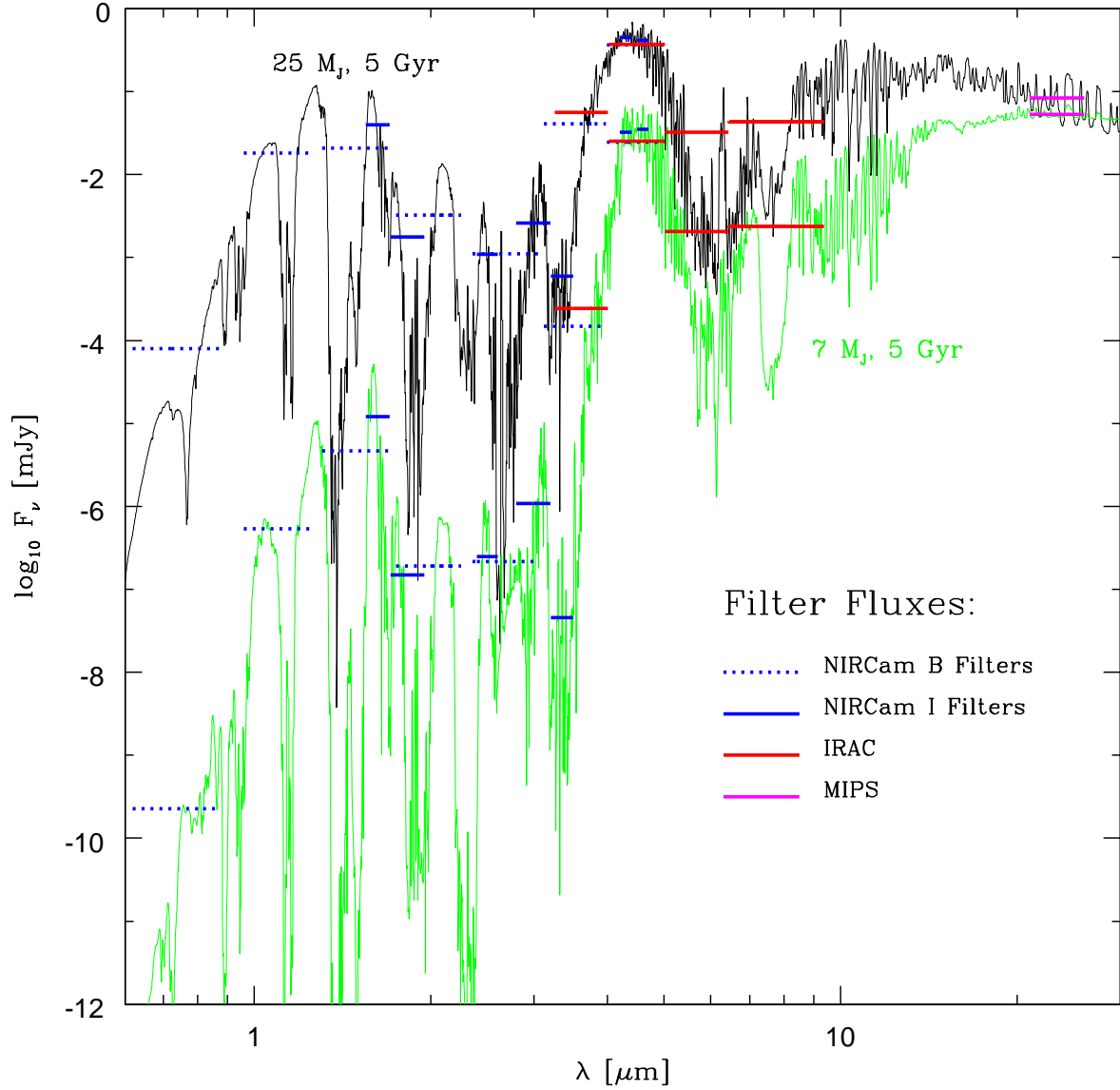


Fig. 12.— Broadband fluxes (in milliJanskys) versus wavelength (in microns) at 10 parsecs for 25- $M_J$  and 7- $M_J$  models at 5 Gyr predicted for SIRTf/IRAC, SIRTf/MIPS, and the NIRCcam B and I filters. Also plotted are the corresponding model spectra (see Fig. 7) from 0.6 to 30  $\mu\text{m}$ .

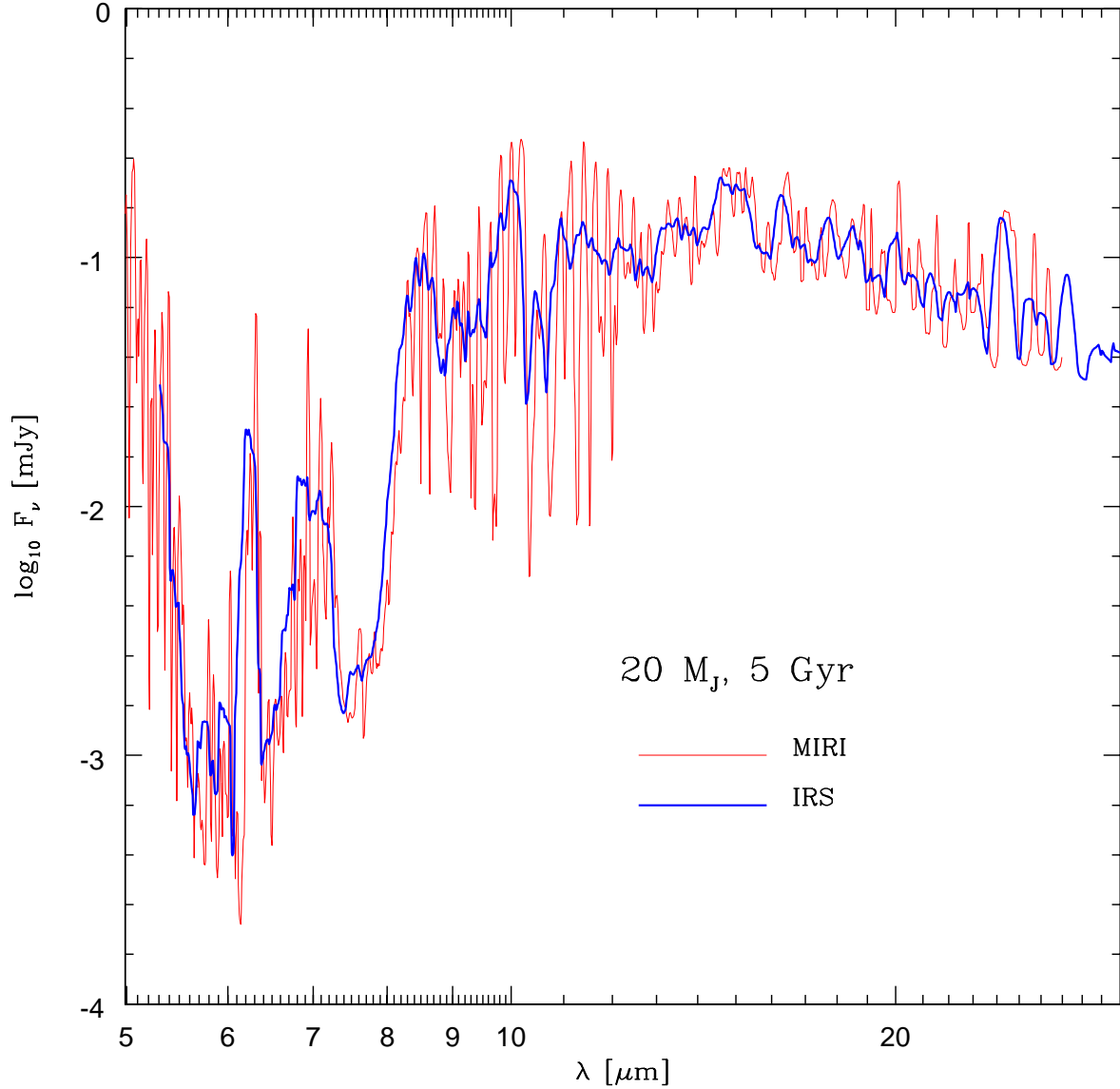


Fig. 13.— The flux spectra (in milliJanskys) versus wavelength (in microns) at 10 parsecs of a 20- $M_J$ , 5-Gyr model deresolved to the SIRTf/IRS (blue) and JWST/MIRI (red) resolutions of 100 and 1000, respectively. With either instrument, the water feature at  $\sim 6.5 \mu\text{m}$ , the methane feature at  $\sim 7.8 \mu\text{m}$ , and the ammonia feature at  $\sim 10.5 \mu\text{m}$  are easily discernible, given adequate signal-to-noise. JWST/MIRI, with its higher spectral resolution, provides more detailed information on band positions and shapes, and, hence, on surface gravity, temperature profile, and composition.

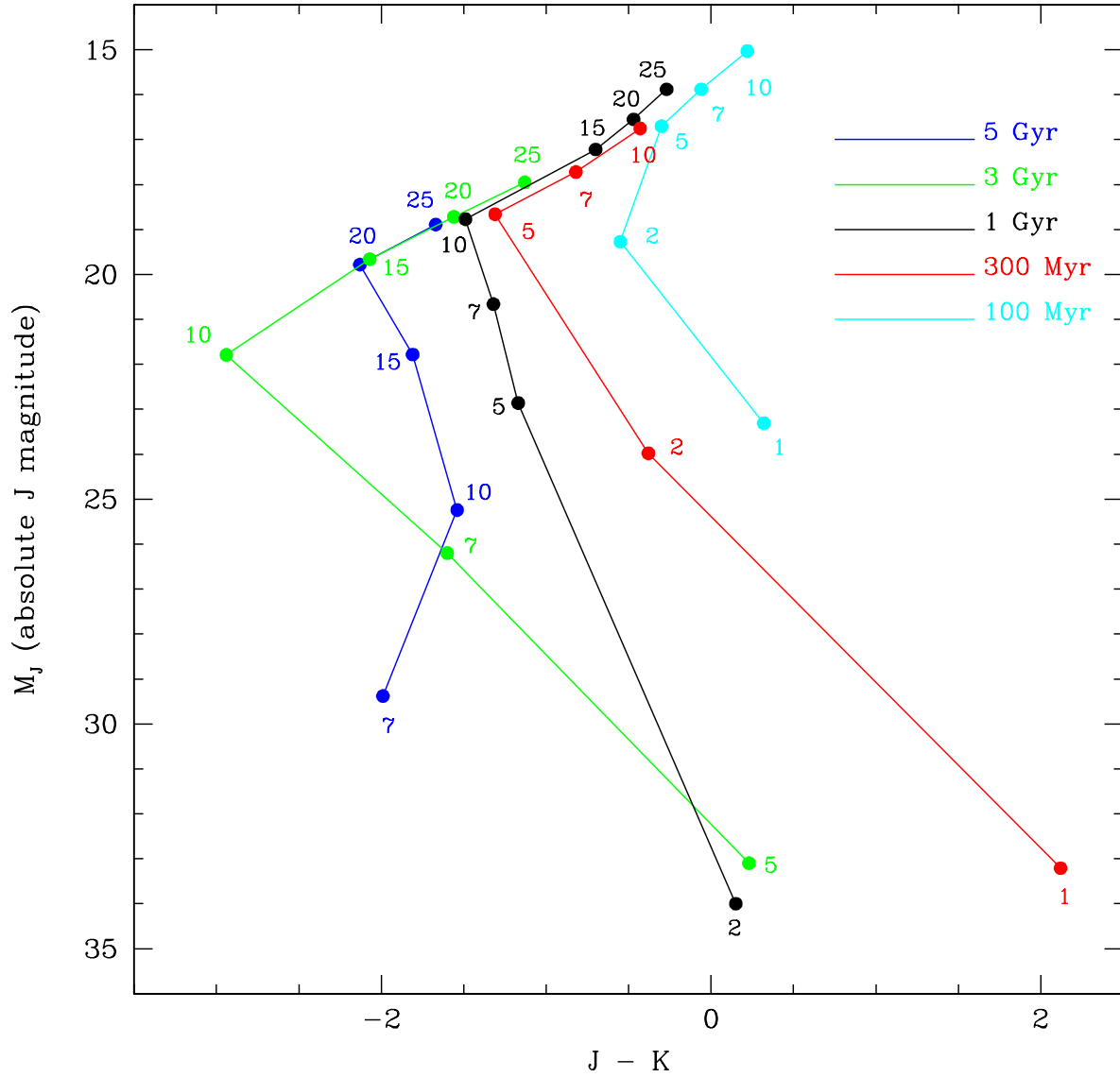


Fig. 14.— Absolute  $J$  magnitude ( $M_J$ ) versus  $J - K$  color for a range of masses and ages. The Bessell color system and filter functions have been used (Bessell and Brett 1988). The numbers by the symbols denote the masses of the objects in Jupiter mass units ( $M_J$ ).